
Flowers: A Warp Drive for Neural PDE Solvers

Till Muser¹ Alexandra Spitzer¹ Matti Lassas² Maarten V. de Hoop³ Ivan Dokmanić¹

Abstract

We introduce FLOWERS, a neural architecture for learning PDE solution operators built entirely from multihead warps. Aside from pointwise channel mixing and a multiscale scaffold, FLOWERS use no Fourier multipliers, no dot-product attention, and no convolutional mixing. Each head predicts a displacement field and warps the mixed input features. Motivated by physics and computational efficiency, displacements are predicted pointwise, without any spatial aggregation, and nonlocality enters *only* through sparse sampling at source coordinates, *one* per head. Stacking warps in multiscale residual blocks yields FLOWERS, which implement adaptive, global interactions at linear cost. We theoretically motivate this design through three complementary lenses: flow maps for conservation laws, waves in inhomogeneous media, and a kinetic-theoretic continuum limit. FLOWERS achieve excellent performance on a broad suite of 2D and 3D time-dependent PDE benchmarks, particularly flows and waves. A compact 17M-parameter model consistently outperforms Fourier, convolution, and attention-based baselines of similar size, while a 150M-parameter variant improves over recent transformer-based foundation models with much more parameters, data, and training compute.

1. Introduction

Deep neural networks have become credible surrogate solvers for PDEs. After training, they run fast, they are differentiable, and they can be conditioned on parameters, forcing, or geometry. What is less settled is what it takes for such models to behave physically rather than as data

¹Department of Mathematics and Computer Science, University of Basel, Basel, Switzerland ²Department of Mathematics and Statistics, University of Helsinki, Helsinki, Finland ³Simons Chair in Computational and Applied Mathematics and Earth Science, Rice University, Houston, TX, USA. Correspondence to: Till Muser <till.muser@unibas.ch>, Ivan Dokmanić <ivan.dokmanic@unibas.ch>.

Preprint. March 6, 2026.

interpolants, to capture qualitative structure, roll out stably, and remain effective across physical regimes.

Most neural PDE backbones rely on Fourier mixing, convolutions, or attention. Fourier layers and attention provide global coupling, but through dense mixing that treats long-range interactions as equally plausible a priori. Convolutions build a locality prior, but interactions are simple linear stencils with weak expressivity at the fringe of the receptive field. For many conservative phenomena $u(t, x)$ depends on *local* interactions between “channels” plus a small set of upstream sources along characteristics or rays, in an adaptive, state-dependent way.

Here we introduce FLOWER, a neural PDE architecture built (near-)exclusively from learned non-linear coordinate warps (or pullbacks). At each target location x , we predict a set of per-head displacements $(\varrho^{(h)}(x))_{h=1}^H$ using only pointwise information at x , and induces nonlocal interaction by sampling features at the displaced coordinates $x + \varrho^{(h)}(x)$. Heads are mixed pointwise and composed in depth and scale. With a fixed number of heads the cost is linear in the number of grid points so scaling to 3D is easy. What we find is somewhat surprising: coordinate warps are a sufficient and scalable primitive to build state-of-the-art neural PDE solvers.

One way to see why warps work is by considering the wave equation. In the high-frequency regime, the solution operator is a Fourier integral operator (FIO): it routes localized wave packets along rays (see Figure 2), which can be read as a sum of pullbacks, or warps, of the initial data. This observation motivated neural networks for waves (Kothari et al., 2020), but it illustrates a common pattern in scientific ML: while models that closely mirror mathematical structure of an operator class usually excel in a narrow set of tasks, they are usually not good neural networks in an engineering sense and thus have limited impact. Here our goal is to extract the key computational primitives from this line of work, guided by physics, and replace the inessential parts with careful deep learning engineering.

Warps are not new in deep learning, but they appear as augmentations of more complex pipelines which involve convolution and/or attention layers (similarly as with FIO networks). The canonical example is the spatial transformer (Jaderberg et al., 2016). The same sampling prim-

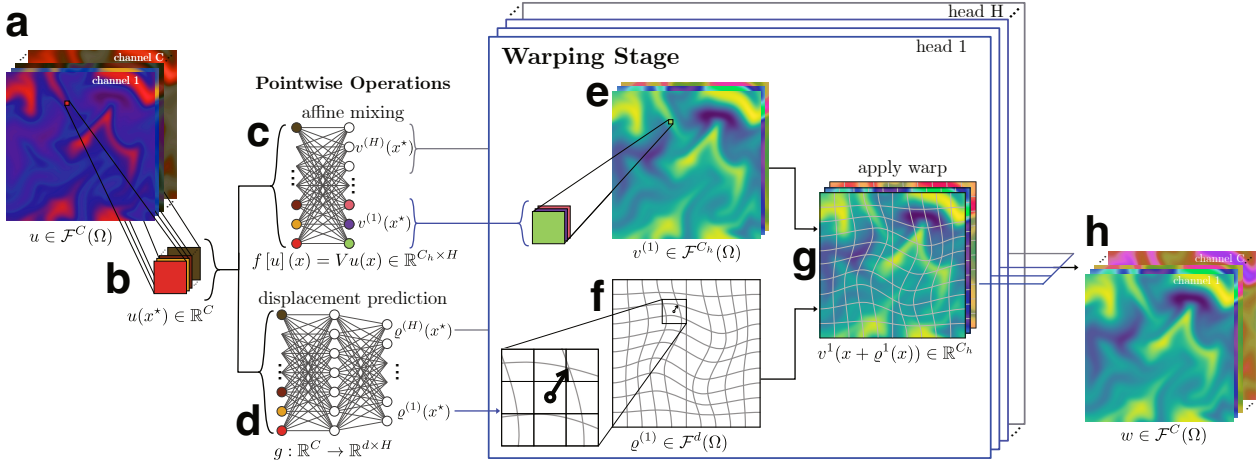


Figure 1. The multi-head SELFWARP layer. (a) Given an input feature map u with C channels, (b) for each pixel x in the image the layer computes (c) a local per-head interaction $v^{(h)}(x) \in \mathbb{R}^{C_h}$ via a linear (affine) projection of the input $u(x)$ and (d) a displacement field (one per head) $\varrho^{(h)}(x)$, also pointwise, using a small MLP. Each C_h -channel per-head interaction field $v^{(h)}$ (e) is warped along the same per-head displacement field $\varrho^{(h)}$ (f) to compute the warped head output (g). The outputs of all heads are concatenated at the output (h).

itive underlies deformable convolutions (Dai et al., 2017), and reappears in deformable transformers (Zhu et al., 2021), where each query predicts a set of sampling offsets, which is shown to improve encoder–decoder object detection transformers. Related ideas have been used for dynamic upsampling (Liu et al., 2023), image registration (Balakrishnan et al., 2019), and scientific forecasting (Zakariaei et al., 2024); in all cases, warping is a component of a convolutional or transformer pipeline.

Motivated by physics, FLOWERS adopt a different perspective. We make warping the *only* adaptive nonlocal mixing primitive: each layer predicts a *single* per-head displacement $\varrho^{(h)}(x)$ using only *pointwise* information at the target location $u(x)$, and induces nonlocal interaction by sampling features at $x + \varrho^{(h)}(x)$, one displacement per head. This keeps the operation lightweight, scalable, and grounded in characteristic structure of PDEs, with nonlocality entering only through sparse pullbacks. We then build a modern backbone around this primitive—multi-head organization, residual connections, and a U-Net-like multiscale scaffold. The empirical takeaway is that this one primitive is enough to obtain state-of-the-art neural PDE solvers across 2D and 3D benchmarks, without Fourier multipliers or dense dot-product attention.

As we show, even a modestly sized FLOWER outperforms strong Fourier-, convolutional-, and attention-based baselines across diverse benchmarks spanning fluid dynamics, wave propagation, and complex geometries. On the *The Well* benchmark suite (Ohana et al., 2025), 17M-parameter FLOWERS achieve state-of-the-art supervised performance while being efficient to train and run. Scaling to ~ 100 –150M parameters closes the gap to, and even improves over,

very recent foundation-scale PDE models trained with far more parameters, data, and compute. (On several datasets even our “tiny” model achieves stronger performance.) This makes FLOWERS a plausible new family of scientific ML backbones, with considerable headroom: we believe that performance will only improve as the community explores the new design space.

1.1. Contributions

- (i) We introduce the SELFWARP layer and the FLOWER architecture, showing how to build effective neural PDE solvers from lightweight pointwise warps.
- (ii) We connect the design of FLOWERS to characteristic/ray structure of solution operators to key PDEs and to a natural kinetic theory (phase space) limit.
- (iii) We show that with a U-Net-like scaffold, FLOWERS outperform strong baselines across datasets and regimes including on almost entire “The Well”.
- (iv) We show that Flower easily scale to 3D. We also show that increasing the number of parameters to 150M makes them competitive with much larger and more resources foundation models.

Finally, we mention that the design of FLOWERS makes them more interpretable than generic architectures. In Figure 6 we show an example of a warp field predicted by a *trained* FLOWER rather than computed “by hand”. It is remarkable that this field indeed “wants to create vortices”.

2. The Flower Architecture

The design of FLOWERS is inspired by the structure of PDEs known as systems of conservation laws. Such sys-

tems are very general and include hydrodynamics (e.g. the Navier–Stokes equations). While the resulting architecture applies well beyond conservation laws, they provide a clean narrative to describe the core mechanics.

We write $u(t, x) \in \mathbb{R}^C$ for the vector of “conserved quantities”, also known as the state, whose evolution we want to predict; for compressible Navier–Stokes, u comprises density, momentum, and energy. A prototypical system is¹

$$\partial_t u(x, t) + \nabla_x \cdot G(u(x, t)) = 0,$$

where $G(u)$ are the so-called fluxes which describe how the conserved quantities flow in space. As we show in Section 3.1, a key component of the solution operators for such systems is a simple pullback, or warp. We now introduce this basic component and the resulting architecture before moving to a more substantial theoretical motivation.

2.1. Architecture

For clarity we present the architecture in continuous coordinates. Let $\Omega \subset \mathbb{R}^d$ be the domain of interest and $\mathcal{F}^C(\Omega) := \{u : \Omega \rightarrow \mathbb{R}^C\}$ the space of C -channel fields on Ω . Given a $\tau : \Omega \rightarrow \mathbb{R}^d$ we define the pullback $(\tau^*v)(x) := v(\tau(x))$. We apply (broadcast) finite-dimensional maps pointwise in the usual way: for a C -channel field u and $h : \mathbb{R}^C \rightarrow \mathbb{R}^{C'}$, we define $(h[u])(x) := h(u(x))$. Concatenation along the channel dimension is denoted $(u \oplus v)(x) = u(x) \oplus v(x)$.

Multihead warp (pullback layer) The main component of FLOWERS is a multihead warp. We begin with a single head. The layer $\text{SELFWARP} : \mathcal{F}^{C_{\text{in}}}(\Omega) \rightarrow \mathcal{F}^{C_{\text{out}}}(\Omega)$ maps a C_{in} -channel input field u to a C_{out} -channel output w as

$$\begin{aligned} w(x) &= \text{SELFWARP}_{V,g}[u](x) \\ &\stackrel{\text{def}}{=} Vu(x + \varrho(x)) \end{aligned}$$

where $\varrho(x) = g(u(x))$; in concise pullback notation,

$$u \mapsto w = (\text{Id} + \varrho)^*(Vu).$$

Crucially, the map $u \mapsto \varrho$ is *local* in a strong sense, i.e. pointwise: $\varrho(x)$ depends on $u(x)$ but not on $u(x')$ for $x' \neq x$. The warping itself is nonlocal and nonlinear, but *sparse*, as it samples the input at a single point.

A single deformation has limited expressivity so we build a multihead variant in the spirit of multihead attention. Fix H heads and $C_{\text{out}} = HC_h$. Let $f(a) = Va$ be a pointwise “value map” and let $g : \mathbb{R}^{C_{\text{in}}} \rightarrow (\mathbb{R}^d)^H$ be a pointwise displacement map with components $g^{(h)}$. For $u \in \mathcal{F}^{C_{\text{in}}}(\Omega)$ define $v := f[u]$ and split it into heads

$$v = v^{(1)} \oplus \dots \oplus v^{(H)} \quad \text{with} \quad v^{(h)} \in \mathcal{F}^{C_h}(\Omega).$$

We then

¹Perhaps augmented with source and diffusive terms.

- (a) predict the H displacement fields,

$$(\varrho^{(1)}, \dots, \varrho^{(H)}) := g[u]$$

We emphasize that (i) each $\varrho^{(h)}$ may depend on *all* input channels (not only channels in head h); and (ii) locality is preserved, i.e., $\varrho^{(h)}(x)$ only depends on $u(x)$ but not $u(x')$ for $x' \neq x$.

- (b) warp, or pull back the input features along the computed displacements,

$$w^{(h)} := (\text{Id} + \varrho^{(h)})^*v^{(h)}$$

- (c) compute output by concatenating the heads

$$\text{SELFWARP}_{V,g}[u] := w^{(1)} \oplus \dots \oplus w^{(H)}.$$

All nonlocality enters through evaluating $v^{(h)}$ at $x + \varrho^{(h)}(x)$, implemented as differentiable interpolation.

Residual pullback block (flower block) We embed the multihead warp in a residual block. Given an input u we first computed a warped update $\text{SELFWARP}_{V,g}[u]$ and add a skip connection via a 1×1 projection,

$$u \mapsto \phi \circ \text{Norm} \circ (\text{Warp}_{V,g}[u] + \text{IdProj})[u]$$

where IdProj is a 1×1 convolution, ϕ is GELU, and Norm is a GroupNorm .

Multiscale composition Simply stacking these residual blocks already yields a strong backbone across a range of forecasting tasks (see Table 8), outperforming baselines and underscoring that learned warps alone are a sufficient primitive for effective PDE solvers. To facilitate modeling multiscale and long-range interactions present in complex dynamics we additionally scaffold FlowerBlocks in a U-Net-like multiscale composition. This is similar to multiscale vision transformers (Liu et al., 2021) and related to classical considerations from numerical PDEs. The details of this construction are laid out in Appendix D. As we show, it leads to the best empirical performance.

3. Theoretical Motivation

Why are FLOWERS a natural architecture for learning solution operators of time-dependent PDEs, especially those governing flows and waves? We sketch three complementary perspectives that connect the architecture to classical structure in PDEs and numerical schemes. These arguments are primarily motivational: we do not claim that any one of those perspectives causally explains the architecture’s empirical success, but together they provide a coherent intuition and suggest routes towards more rigorous theory. Our hope is that the reader will find at least one of the three vignettes helpful and illuminating.

3.1. Scalar conservation laws

Consider a scalar conservation law for u ,

$$\begin{cases} \partial_t u(t, x) + \nabla_x \cdot (G(u(t, x))) = 0, & u(0, x) = u^0(x), \\ u : \mathbb{R}_+ \times \mathbb{R}^d \rightarrow \mathbb{R}, & G : \mathbb{R} \rightarrow \mathbb{R}^d. \end{cases}$$

Canonical examples include the Burgers equation and traffic-flow models. Since G depends on x only through $u(t, x)$, the chain rule yields the equivalent quasilinear transport form, sometimes called a nonlinear optical flow (Aubert & Kornprobst, 2006),

$$\partial_t u(t, x) + A(u(t, x)) \cdot \nabla_x u(t, x) = 0$$

where $A(u) = \frac{d}{du}G(u)$. This lets us introduce characteristics: define $\Phi_t(x)$ by

$$\partial_t \Phi_t(x) = A(u(t, \Phi_t(x))), \quad \Phi_0(x) = x.$$

As long as a classical solution exists (i.e., prior to shock formation), u is constant along characteristics,

$$u(t, \Phi_t(x)) = u(0, x).$$

Equivalently,

$$u(t, x) = (\Phi_t^{-1})^* u^0(x).$$

More generally, writing $\Phi_{t \leftarrow s} \stackrel{\text{def}}{=} \Phi_t \circ \Phi_s^{-1}$ for the flow map from time s to t , we have

$$u(t, \cdot) = (\Phi_{t \leftarrow s}^{-1})^* u(s, \cdot).$$

The relevance to FLOWERS is immediate: the solution operator (locally in time) is a pullback of the state by a warping map $\Phi_{t \leftarrow s}^{-1}$. More can be said. Over a short step Δt we have the expansion

$$\Phi_{t+\Delta t \leftarrow t}^{-1}(x) = x - \Delta t A(u(t, x)) + O(\Delta t^2)$$

so to first order the displacement needed to compute $u(t + \Delta t, x)$ only depends on the *local* state $u(t, x)$, not on values $u(t, x')$ at other locations $x' \neq x$. This is precisely what our SELFWARP primitive does.

Figure 6 provides empirical evidence: on the shear flow dataset, the learned displacements visibly align with the underlying fluid velocity, suggesting that FLOWER discovers physically meaningful transport directions. From a deep learning engineering point of view, the locality of the flow map results in parameter and compute efficiency.

Generalizing these ideas to systems of conservation laws—especially those with constraints and additional structure, as in compressible Euler and Navier–Stokes—is substantially more delicate. In Appendix B we outline how FLOWERS can express the requisite components (multiple characteristic families, coupling, and source-like effects), by employing more than one head. In the next section we outline a different, wave perspective which requires multiple heads.

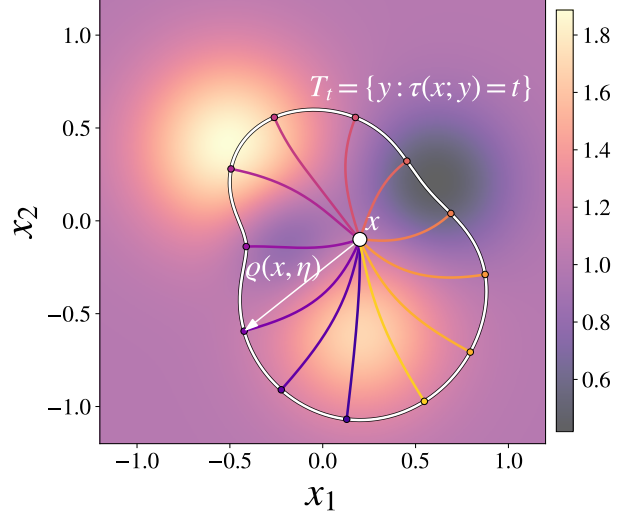


Figure 2. Wavefronts and rays picture: high-frequency waves propagate along rays. The solution at position x and time t is a sum of contributions along the wavefront, which can be indexed by head η .

3.2. Waves and geometric optics

Consider the variable-speed wave equation

$$\partial_t^2 u - c(x)^2 \Delta u = 0,$$

with Cauchy data $u(0, \cdot) = u_0$, $\partial_t u(0, \cdot) = u_1$. In the geometric-optics regime (and away from caustics), the solution at (t, x) is well approximated by a superposition of contributions arriving along rays. Equivalently, writing $\Gamma_{-t}(x, \eta)$ for the point reached by tracing a ray *backwards* from x for time t with initial direction $\eta \in \mathbb{S}^{d-1}$, one obtains the pullback representation

$$\begin{aligned} u(t, x) \approx & \int_{\mathbb{S}^{d-1}} \widehat{W}_0(t, x, \eta) u_0(\Gamma_{-t}(x, \eta)) d\eta \\ & + \int_{\mathbb{S}^{d-1}} \widehat{W}_1(t, x, \eta) u_1(\Gamma_{-t}(x, \eta)) d\eta. \end{aligned} \quad (1)$$

for smooth weights $\widehat{W}_{0,1}$ (absorbing Jacobian/amplitude factors); Appendix F derives this standard parametrization from a Green’s function/WKB ansatz.

Equation (1) matches a *multihead pullback* layer: each head samples the input at a displaced coordinate, and pointwise channel mixing supplies the weights. Approximating the angular integral by a learned quadrature yields

$$\sum_{h=1}^H \alpha_{0,1}^{(h)}(t, x) u_{0,1}(\Gamma_{-t}(x, \eta^{(h)}(t, x))), \quad (2)$$

i.e., a sum of pullbacks. In FLOWERS, both the effective directions $\eta^{(h)}$ (\equiv displacements) and weights $\alpha^{(h)}$ are produced *pointwise* from local lifted features at x (state, coefficients/geometry channels, coordinates, and metadata such

as Δt), yielding an adaptive alternative to uniform angular discretization. Multiple heads also naturally represent multiple arrivals/branches, with subsequent local mixing modeling interference and mode coupling.

3.3. A kinetic theory perspective

Our third perspective is the natural continuum limit of FLOWERS. In this limit, the architecture can be interpreted as a discretization of a generalized Boltzmann-type equation, with a key twist: the streaming velocity is *self-adaptive*, i.e., it depends on the current lifted state over heads. This viewpoint is appealing because such kinetic (Boltzmann/Vlasov-type) equations serve as “master” descriptions from which many macroscopic models—including hydrodynamics—can be derived via suitable moments and closures. Moreover, the related kinetic numerical schemes such as the lattice-Boltzmann method (Krüger et al., 2017) have a stream-and-collide (\equiv locally interact) structure similar to FLOWERS (Benitez et al., 2025).

We work formally and refer to Appendix E for details. Consider a single-scale cascade of flower blocks indexed by $n = 0, \dots, N$, with time step $\Delta t \stackrel{\text{def}}{=} T/N$ and $t_n \stackrel{\text{def}}{=} n\Delta t$. We take a regime in which the number of heads grows and the discrete head index can be replaced by a continuous phase variable $\eta \in \mathbb{R}^k$ (more generally, η may live on a manifold that parameterizes transport modes). The network state becomes a lifted field $u_n(x, \eta)$, and in the joint limit $N \rightarrow \infty$, $\Delta t \rightarrow 0$ (with appropriate scaling of the per-layer displacements), one obtains a continuum evolution $u_n(x, \eta) \rightarrow u(t, x, \eta)$ governed by

$$\begin{aligned} \partial_t u(t, x, \eta) + \mathcal{B}(\eta; u(t, x, \cdot)) \cdot \nabla_x u(t, x, \eta) \\ = \mathcal{Q}_t(\eta; u(t, x, \cdot)). \end{aligned} \quad (3)$$

Here \mathcal{B} plays the role of a streaming (transport) velocity, while \mathcal{Q}_t is an interaction term capturing local channel mixing, head coupling, and any additional pointwise nonlinearities. A notable distinction from the classical Boltzmann equation is that \mathcal{B} is not fixed by an a priori velocity variable: it is predicted from the lifted state $u(t, x, \cdot)$ itself, enabling the transport directions and speeds to adapt to the evolving solution.

This suggests a very nice interpretation of heads as a phase-space lift: the phase variable η indexes transport modes, and FLOWERS can be viewed as learning dynamics in a lifted phase space (x, η) before projecting back to physical space. In particular, macroscopic quantities can be recovered as moments or learned projections over η , which parallels the kinetic-to-hydrodynamic viewpoint, while the adaptive streaming provides additional expressive power beyond standard fixed-velocity kinetic models.

4. Results

In this section we evaluate FLOWER on a diverse suite of operator-learning benchmarks drawn from The Well (Ohana et al., 2025) and additional collections, and compare against strong baselines. Table 1 is the main quantitative comparison; Figures 3–5 give representative qualitative comparisons, including next-step predictions in challenging rheology (viscoelastic instability), autoregressive rollouts, and 3D buoyancy-driven dynamics (Rayleigh–Taylor).

We organize the experiments as follows:

- Section 4.1 benchmarks 15–20M parameter models on unconditioned $4 \rightarrow 1$ next-step prediction, following the evaluation protocol of The Well.
- Section 4.2 studies scaling to larger networks and compares against a recent very large foundation model for PDEs (Herde et al., 2024).
- Section 4.3 ablates key architectural choices in FLOWERS.

Additional results are deferred to the appendix, including a conditioned $1 \rightarrow 1$ task with simulation parameters provided separately (Table 7) and a time-independent PDE benchmark (Table 4, Figure 11).

4.1. 4-to-1 Benchmarking

We start with The Well benchmark, where the goal is to predict the state at time index n from the previous four frames u_{n-4}, \dots, u_{n-1} . A key difficulty is that each dataset contains trajectories from the *same* underlying PDE family but with varying simulation parameters (e.g., coefficients, boundary or forcing settings). These parameters are *not* provided to the model and must therefore be inferred implicitly from the short history window, making the task both a forecasting and a latent system-identification problem (Ruiz et al., 2025).

Table 1 summarizes next-step prediction performance across 16 datasets with diverse physics. FLOWER achieves the lowest error overall and is typically best by a substantial margin. This in particular indicates robustness to parameter variation within each PDE family.

We next evaluate long-horizon behavior via autoregressive rollouts: we iteratively apply the one-step predictor to generate extended trajectories. The rollout results (second block of columns in Table 1) largely mirror the one-step ranking: FLOWER remains best on most datasets, with the main exception of the neutron star merger aftermath simulation, where it is slightly outperformed by FNO.

Finally, these accuracy gains come with high practical throughput. As shown in Figure 7, FLOWER matches or exceeds the throughput of FNO and SCOT across resolutions, while substantially outperforming CNEXTU-NET,

Collection	Dataset	Next-step				1:20 Rollout			
		<i>FNO</i>	<i>CNUNET</i>	<i>SCOT</i>	<i>FLOWER</i>	<i>FNO</i>	<i>CNUNET</i>	<i>SCOT</i>	<i>FLOWER</i>
The Well	acoustic_scattering_maze	0.1454	0.0129	0.0361	0.0064	0.4197	0.0874	0.1996	0.0489
	active_matter	0.1749	0.0650	0.1050	0.0249	3.2862	1.7781	4.1055	1.3905
	gray_scott_reaction_diffusion	0.0372	0.0188	0.0673	0.0102	0.9125	0.3059	0.4169	0.2074
	MHD_64	0.3403	0.2062	–	0.1165	1.3007	0.9534	–	0.7580
	planetswe	0.0070	0.0027	0.0041	0.0007	0.1316	0.0624	0.0518	0.0187
	post_neutron_star_merger	0.4452	0.3391	–	0.3269	0.5980	0.6529	–	0.6223
	rayleigh_benard	0.2104	0.2171	0.1863	0.0807	39.038	12.507	5.6486	2.1661
	rayleigh_taylor_instability	0.1714	0.1351	–	0.0491	3.0057	5.3894	–	0.5862
	shear_flow	0.0769	0.0594	0.1093	0.0463	1.1245	0.7632	0.8930	0.2246
	supernova_explosion	0.4326	0.4316	–	0.2888	1.0162	2.2913	–	0.8113
	turbulence_gravity_cooling	0.2720	0.2113	–	0.1700	3.2583	2.0510	–	1.2636
	turbulent_radiative_layer_2D	0.3250	0.2559	0.3555	0.1930	1.2328	0.7051	0.8299	0.5491
	turbulent_radiative_layer_3D	0.3261	0.3322	–	0.2073	0.9203	0.7139	–	0.6840
viscoelastic_instability [†]	0.1914	0.1623	0.2017	0.0624	0.4284	0.3592	0.4890	0.3465	
PDEBench	Diffusion-Reaction	0.0191	0.0033	0.0150	0.0015	0.7563	0.0279	0.0949	0.0241
	Shallow Water	0.0019	0.0044	0.0187	0.0010	0.2499	0.1427	0.1164	0.0076

Table 1. VRMSE for unconditioned 4→1 next-step prediction and 1:20 rollout. Best in bold, second best colored green. [†]Using a fixed viscoelastic_instability dataset, see A.3.

especially in 3D.

4.2. Scaling FLOWERS

We next study how FLOWER scales on the Euler multi quadrants (periodic) dataset from The Well. Beyond the 17M-parameter model used throughout the main benchmark (FLOWER-Tiny), we train two larger variants: FLOWER-Small (70M parameters) and FLOWER-Medium (156M parameters). All models are trained from scratch for 40 epochs; in wall-clock terms this corresponds to roughly a week of training on 1, 2, and 4 H200 GPUs, respectively. We compare with POSEIDON-L (Herde et al., 2024), a large foundation model based on the SCOT architecture, pre-trained on a diverse collection of fluid-dynamics problems. This model was similarly trained for 40 epochs on 4 H200s.

Table 2 reports the resulting errors. Performance improves smoothly with model size, indicating that FLOWER can indeed benefit from the additional capacity, without a change in training recipe or architecture class. We also note that

Model	Parameters	1-Step	1:20 Rollout
FLOWER-Tiny	17.3M	0.0160	0.1114
FLOWER-Small	69.3M	0.0124	0.0850
FLOWER-Medium	155.8M	0.0108	0.0739
POSEIDON-L	628.6M	0.0194	0.1114

Table 2. Model scaling study on an compressible Euler equations dataset, loss given as VRMSE.

even a tiny FLOWER delivers results comparable to a large attention-based model.

4.3. Ablations

We ablate FLOWER on the viscoelastic instability dataset to assess which components matter in practice. Table 3 reports one-step prediction error and 1:20 autoregressive rollout error (VRMSE), with variants sorted by rollout performance.

Warping is clearly non-negotiable. Removing it leaves a U-Net-like multiscale backbone without a spatial interaction mechanism, and error increases dramatically. Interestingly, a *single-head* warp already recovers much of the gain for one-step prediction; indeed it is competitive with (and here exceeds) CNUNET. This is consistent with the conservation-law viewpoint in Appendix B: a single locally predicted deformation can capture a substantial part of a transport-dominated update. Conversely, even without the U-net scaffold, a single-scale FLOWER operating at fixed resolution remains competitive with baselines (Table 8).

For long-horizon rollouts, however, a single head is not sufficient: it yields poor 1:20 error even when one-step performance is reasonable. Multiple heads are therefore important for stability and accuracy over repeated composition, likely because they allow the model to represent several concurrently active transport modes rather than forcing a single displacement field to explain all motion.

Other components have smaller but consistent effects. Coordinate encodings in the lifted representation improve both

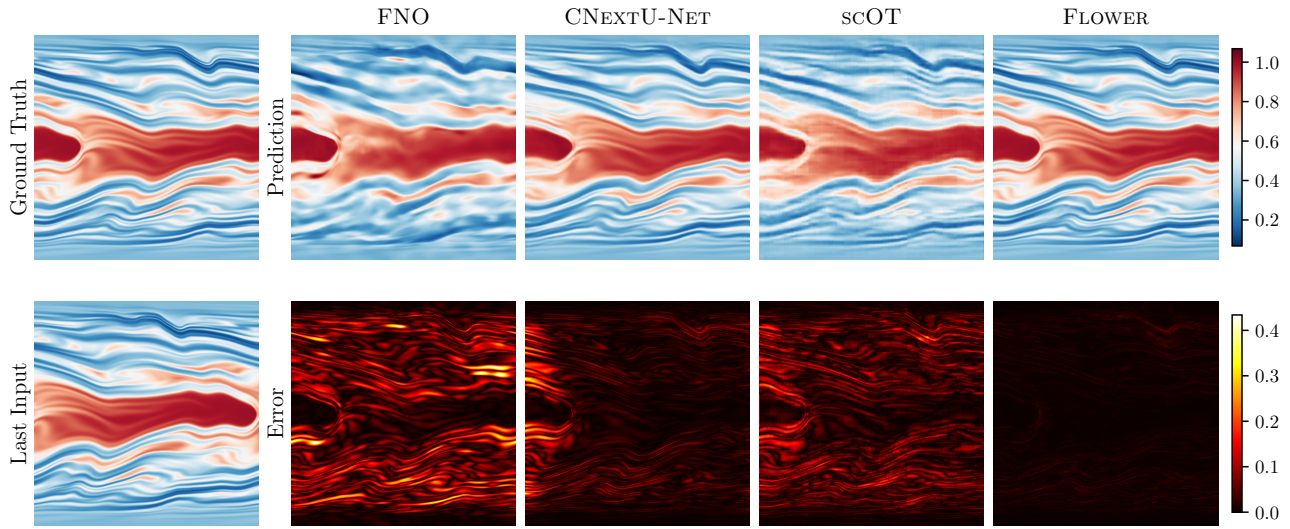


Figure 3. Comparison of model predictions on the viscoelastic instability dataset (4→1 unconditioned setting), showing the conformation tensor entry C_{zz} . The top row shows the ground truth and the prediction of each model, bottom row shows the last of the four input frames and prediction errors.

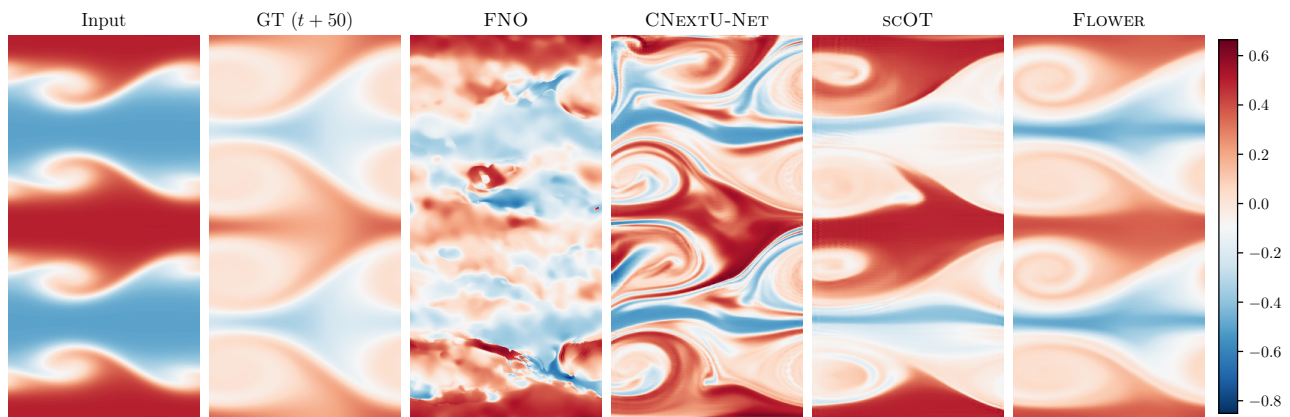


Figure 4. Comparison of autoregressive rollout model predictions on the shear flow dataset (4→1 unconditioned setting), showing the tracer.

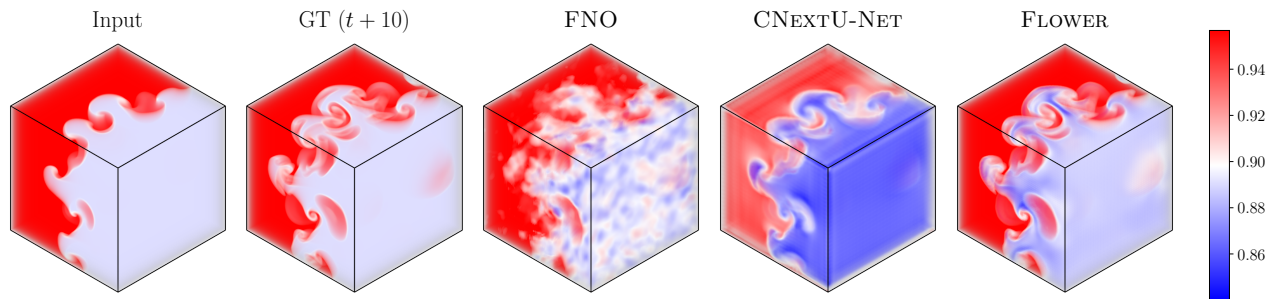


Figure 5. Comparison of model predictions on the Rayleigh-Taylor instability dataset (4→1 unconditioned setting), showing the density. Visualized using vape4d (Koehler et al., 2024).

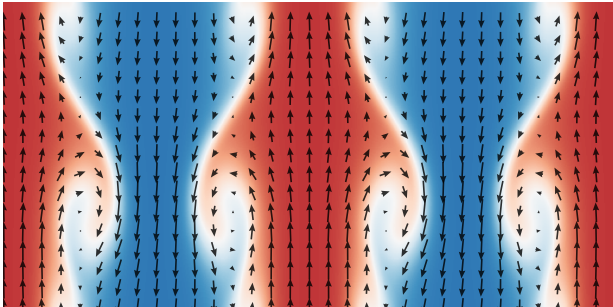


Figure 6. Visualization of a learned self-warp for the Shear Flow dataset (cf. Fig. 4). The black arrows show the learned displacement field $\varrho^{(1)}(x)$ of the first head in FLOWER’s first downsampling block, overlaid on the tracer field. Without explicit supervision, the model learns displacements that align remarkably well with the underlying fluid velocity, providing evidence that the strong performance of FLOWER comes from discovering physically-meaningful transport directions.

one-step and rollout performance, indicating that geometric context is useful even when displacements are predicted pointwise. Replacing the displacement MLP with a single convolution degrades results, suggesting that the headwise motion benefits from richer pointwise nonlinearities. Finally, the residual projection (IdProj) and normalization mainly affect rollouts: removing IdProj or GroupNorm typically worsens 1:20 performance, even when the one-step metric changes only modestly. Notably, omitting GroupNorm slightly improves one-step error while harming rollouts, consistent with normalization primarily stabilizing repeated composition.

We emphasize that the relative importance of these components depends on the problem. For example, coordinate encodings may matter more with complex boundaries or discontinuous coefficients. Likewise, multiple heads should matter more when several transport families are active (e.g., multi-field coupling, mixed wave types, or strongly heterogeneous media).

Model Variant	1-Step	1:20 Rollout
w/o warping	0.4974	0.6911
single-head flow	0.1241	0.6719
w/o coord encoding in lift	0.0638	0.4065
single conv flow (no MLP)	0.0834	0.3998
w/o IdProj	0.0712	0.3816
w/o GroupNorm	0.0622	0.3760
Full Model	0.0624	0.3465
vs. CUNET	0.1623	0.3592

Table 3. Ablation study on FLOWER components, evaluated on the viscoelastic instability dataset (via VRMSE loss), sorted by 1:20 rollout loss. CUNET values given for comparison.

5. Discussion

Our experimental results show that multihead warping is a strong primitive for PDE learning on a broad range of phenomena. It yields lower error in forecasting complex dynamics than baselines of comparable size, and sometimes than much larger and much more resourced models. It also scales well and admits high throughput at high resolution, even in 3D, which is often challenging.

5.1. Limitations

What we understand reasonably well is why warps are a natural mechanism for waves and flows: characteristics for conservation laws and rays in geometric optics both imply pullback-like updates, and the continuum limit offers a kinetic view in which heads index transport modes. What we do *not* understand is when the learned warps align with physically meaningful transports, how the architecture handles non-hyperbolic physics, and how to stabilize rollouts which are currently not great.

Indeed, while FLOWERS can outperform larger models on transport-dominated phenomena, they do not reach Poseidon (Herde et al., 2024) and Walrus (McCabe et al., 2025) on more diffusive problems like Gray–Scott and active matter. They do, however, outperform strong baselines of comparable size on those problems and we currently do not have a great explanation why. Warps can implement convolutions and averaging but whether that is what is going on remains to be understood. Even more mystifying is solid performance on the time-independent Helmholtz equation (Table 4), where we lack a satisfying explanation. This means that our motivational vignettes should be read as intuition builders but not as explanations.

Acknowledgements

ML was partially supported by the Advanced Grant project 101097198 of the European Research Council, Centre of Excellence of Research Council of Finland (grant 336786) and the FAME flagship of the Research Council of Finland (grant 359186). The views and opinions expressed are those of the authors only and do not necessarily reflect those of the funding agencies or the EU. MVdH gratefully acknowledges the support of the Department of Energy, BES program under grant DE-SC0020345, Oxy, the corporate members of the Geo-Mathematical Imaging Group at Rice University and the Simons Foundation under the MATH+X Program. TM would like to thank Lilian Gasser for the considerable time and expertise she dedicated to the design of Figure 1.

Impact Statement

This paper presents work whose goal is to advance the field of Machine Learning. There are many potential societal consequences of our work, none which we feel must be specifically highlighted here.

References

- Aubert, G. and Kornprobst, P. *Mathematical problems in image processing*, volume 147 of *Applied Mathematical Sciences*. Springer, New York, second edition, 2006. ISBN 978-0387-32200-1; 0-387-32200-0. Partial differential equations and the calculus of variations, With a foreword by Olivier Faugeras.
- Balakrishnan, G., Zhao, A., Sabuncu, M. R., Guttag, J., and Dalca, A. V. Voxelmorph: A learning framework for deformable medical image registration. *IEEE Transactions on Medical Imaging*, 38(8):1788–1800, August 2019. ISSN 1558-254X. doi: 10.1109/tmi.2019.2897538. URL <http://dx.doi.org/10.1109/TMI.2019.2897538>.
- Beneitez, M., Page, J., Dubief, Y., and Kerswell, R. R. Multistability of elasto-inertial two-dimensional channel flow. *Journal of Fluid Mechanics*, 981:A30, 2024.
- Benitez, J., Hegazy, K., Guo, J., Dokmanić, I., Mahoney, M. W., and de Hoop, M. V. Neural equilibria for long-term prediction of nonlinear conservation laws. *arXiv preprint arXiv:2501.06933*, 2025.
- Bhatnagar, S., Afshar, Y., Pan, S., Duraisamy, K., and Kaushik, S. Prediction of aerodynamic flow fields using convolutional neural networks. *Computational Mechanics*, 64(2):525–545, 2019. doi: 10.1007/s00466-019-01740-0. URL <https://doi.org/10.1007/s00466-019-01740-0>.
- Burkhart, B., Appel, S., Bialy, S., Cho, J., Christensen, A., Collins, D., Federrath, C., Fielding, D., Finkbeiner, D., Hill, A., et al. The catalogue for astrophysical turbulence simulations (cats). *The Astrophysical Journal*, 905(1):14, 2020.
- Burns, K. J., Vasil, G. M., Oishi, J. S., Lecoanet, D., and Brown, B. P. Dedalus: A flexible framework for numerical simulations with spectral methods. *Physical Review Research*, 2(2):023068, 2020.
- Cao, S. Choose a transformer: Fourier or galerkin, 2021. URL <https://arxiv.org/abs/2105.14995>.
- Curtis, S., Miller, J. M., Fröhlich, C., Sprouse, T., Lloyd-Ronning, N., and Mumpower, M. Nucleosynthesis in outflows from black hole–neutron star merger disks with full gr (ν) rmhd. *The Astrophysical Journal Letters*, 945(1):L13, 2023.
- Dai, J., Qi, H., Xiong, Y., Li, Y., Zhang, G., Hu, H., and Wei, Y. Deformable convolutional networks, 2017. URL <https://arxiv.org/abs/1703.06211>.
- Dosovitskiy, A., Beyer, L., Kolesnikov, A., Weissenborn, D., Zhai, X., Unterthiner, T., Dehghani, M., Minderer, M., Heigold, G., Gelly, S., Uszkoreit, J., and Houshy, N. An image is worth 16x16 words: Transformers for image recognition at scale, 2021. URL <https://arxiv.org/abs/2010.11929>.
- Fielding, D. B., Ostriker, E. C., Bryan, G. L., and Jermyn, A. S. Multiphase gas and the fractal nature of radiative turbulent mixing layers. *The Astrophysical Journal Letters*, 894(2):L24, 2020.
- Guibas, J., Mardani, M., Li, Z., Tao, A., Anandkumar, A., and Catanzaro, B. Adaptive fourier neural operators: Efficient token mixers for transformers, 2022. URL <https://arxiv.org/abs/2111.13587>.
- Hao, Z., Wang, Z., Su, H., Ying, C., Dong, Y., Liu, S., Cheng, Z., Song, J., and Zhu, J. Gnot: A general neural operator transformer for operator learning. In *International Conference on Machine Learning*, pp. 12556–12569. PMLR, 2023.
- Hao, Z., Su, C., Liu, S., Berner, J., Ying, C., Su, H., Anandkumar, A., Song, J., and Zhu, J. Dpot: Auto-regressive denoising operator transformer for large-scale pde pre-training, 2024. URL <https://arxiv.org/abs/2403.03542>.
- Herde, M., Raonić, B., Rohner, T., Käppeli, R., Molinaro, R., de Bézenac, E., and Mishra, S. Poseidon: Efficient foundation models for pdes, 2024. URL <https://arxiv.org/abs/2405.19101>.
- Hirashima, K., Moriwaki, K., Fujii, M. S., Hirai, Y., Saitoh, T. R., and Makino, J. 3d-spatiotemporal forecasting the expansion of supernova shells using deep learning towards high-resolution galaxy simulations. *Monthly Notices of the Royal Astronomical Society*, 526(3):4054–4066, 2023a.
- Hirashima, K., Moriwaki, K., Fujii, M. S., Hirai, Y., Saitoh, T. R., Makino, J., and Ho, S. Surrogate modeling for computationally expensive simulations of supernovae in high-resolution galaxy simulations. *arXiv preprint arXiv:2311.08460*, 2023b.
- Jaderberg, M., Simonyan, K., Zisserman, A., and Kavukcuoglu, K. Spatial transformer networks, 2016. URL <https://arxiv.org/abs/1506.02025>.

- Koehler, F., Niedermayr, S., Westermann, R., and Thuerey, N. APEBench: A benchmark for autoregressive neural emulators of PDEs. *Advances in Neural Information Processing Systems (NeurIPS)*, 38, 2024.
- Kossaifi, J., Kovachki, N., Li, Z., Pitt, D., Liu-Schiaffini, M., George, R. J., Bonev, B., Azizzadenesheli, K., Berner, J., and Anandkumar, A. A library for learning neural operators, 2024.
- Kothari, K., de Hoop, M., and Dokmanić, I. Learning the geometry of wave-based imaging, 2020. URL <https://arxiv.org/abs/2006.05854>.
- Kovachki, N., Li, Z., Liu, B., Azizzadenesheli, K., Bhattacharya, K., Stuart, A., and Anandkumar, A. Neural operator: Learning maps between function spaces with applications to pdes. *Journal of Machine Learning Research*, 24(89):1–97, 2023.
- Kovachki, N. B., Li, Z., Liu, B., Azizzadenesheli, K., Bhattacharya, K., Stuart, A. M., and Anandkumar, A. Neural operator: Learning maps between function spaces. *CoRR*, abs/2108.08481, 2021.
- Krüger, T., Kusumaatmaja, H., Kuzmin, A., Shardt, O., Silva, G., and Viggen, E. M. *The Lattice Boltzmann Method*. Springer International Publishing, 2017. doi: 10.1007/978-3-319-44649-3. URL <http://dx.doi.org/10.1007/978-3-319-44649-3>.
- Li, Z., Kovachki, N., Azizzadenesheli, K., Liu, B., Bhattacharya, K., Stuart, A., and Anandkumar, A. Neural operator: Graph kernel network for partial differential equations, 2020. URL <https://arxiv.org/abs/2003.03485>.
- Li, Z., Kovachki, N., Azizzadenesheli, K., Liu, B., Bhattacharya, K., Stuart, A., and Anandkumar, A. Fourier neural operator for parametric partial differential equations, 2021. URL <https://arxiv.org/abs/2010.08895>.
- Li, Z., Meidani, K., and Farimani, A. B. Transformer for partial differential equations’ operator learning. *arXiv preprint arXiv:2205.13671*, 2022.
- Li, Z., Kovachki, N. B., Choy, C., Li, B., Kossaifi, J., Otta, S. P., Nabian, M. A., Stadler, M., Hundt, C., Azizzadenesheli, K., and Anandkumar, A. Geometry-informed neural operator for large-scale 3d pdes, 2023. URL <https://arxiv.org/abs/2309.00583>.
- Liu, T., Benitez, J. A. L., Faucher, F., Khorashadizadeh, A., de Hoop, M. V., and Dokmanić, I. WaveBench: Benchmarking data-driven solvers for linear wave propagation PDEs. *Transactions on Machine Learning Research*, 2024. ISSN 2835-8856. URL <https://openreview.net/forum?id=6wpInwnzs8>.
- Liu, W., Lu, H., Fu, H., and Cao, Z. Learning to upsample by learning to sample. In *Proceedings of the IEEE/CVF international conference on computer vision*, pp. 6027–6037, 2023.
- Liu, Z., Lin, Y., Cao, Y., Hu, H., Wei, Y., Zhang, Z., Lin, S., and Guo, B. Swin transformer: Hierarchical vision transformer using shifted windows, 2021. URL <https://arxiv.org/abs/2103.14030>.
- Loshchilov, I. and Hutter, F. Decoupled weight decay regularization, 2019. URL <https://arxiv.org/abs/1711.05101>.
- Lu, L., Jin, P., Pang, G., Zhang, Z., and Karniadakis, G. E. Learning nonlinear operators via deepoNet based on the universal approximation theorem of operators. *Nature Machine Intelligence*, 3(3):218–229, March 2021. ISSN 2522-5839. doi: 10.1038/s42256-021-00302-5. URL <http://dx.doi.org/10.1038/s42256-021-00302-5>.
- Lund, K. A., McLaughlin, G. C., Miller, J. M., and Mumpower, M. R. Magnetic field strength effects on nucleosynthesis from neutron star merger outflows. *The Astrophysical Journal*, 964(2):111, 2024.
- Luo, H., Wu, H., Zhou, H., Xing, L., Di, Y., Wang, J., and Long, M. Transolver++: An accurate neural solver for pdes on million-scale geometries, 2025. URL <https://arxiv.org/abs/2502.02414>.
- Maddu, S., Weady, S., and Shelley, M. J. Learning fast, accurate, and stable closures of a kinetic theory of an active fluid. *Journal of Computational Physics*, 504: 112869, 2024.
- Mandli, K. T., Ahmadi, A. J., Berger, M., Calhoun, D., George, D. L., Hadjimichael, Y., Ketcheson, D. I., Lemoine, G. I., and LeVeque, R. J. Clawpack: building an open source ecosystem for solving hyperbolic pdes. *PeerJ Computer Science*, 2:e68, 2016.
- McCabe, M., Harrington, P., Subramanian, S., and Brown, J. Towards stability of autoregressive neural operators. *arXiv preprint arXiv:2306.10619*, 2023.
- McCabe, M., Blancard, B. R.-S., Parker, L. H., Ohana, R., Cranmer, M., Bietti, A., Eickenberg, M., Golkar, S., Krawezik, G., Lanusse, F., Pettee, M., Tesileanu, T., Cho, K., and Ho, S. Multiple physics pretraining for physical surrogate models, 2024. URL <https://arxiv.org/abs/2310.02994>.
- McCabe, M., Mukhopadhyay, P., Marwah, T., Blancard, B. R.-S., Rozet, F., Diaconu, C., Meyer, L., Wong, K. W. K., Sotoudeh, H., Bietti, A., Espejo, I., Fear, R., Golkar, S., Hehir, T., Hirashima, K., Krawezik, G., Lanusse, F.,

- Morel, R., Ohana, R., Parker, L., Pettee, M., Shen, J., Cho, K., Cranmer, M., and Ho, S. Walrus: A cross-domain foundation model for continuum dynamics, 2025. URL <https://arxiv.org/abs/2511.15684>.
- Miller, J. M., Ryan, B. R., and Dolence, J. C. ν bhlight: radiation grmhd for neutrino-driven accretion flows. *The Astrophysical Journal Supplement Series*, 241(2):30, 2019a.
- Miller, J. M., Ryan, B. R., Dolence, J. C., Burrows, A., Fontes, C. J., Fryer, C. L., Korobkin, O., Lippuner, J., Mumpower, M. R., and Wollaeger, R. T. Full transport model of gw170817-like disk produces a blue kilonova. *Physical Review D*, 100(2):023008, 2019b.
- Miller, J. M., Sprouse, T. M., Fryer, C. L., Ryan, B. R., Dolence, J. C., Mumpower, M. R., and Surman, R. Full transport general relativistic radiation magnetohydrodynamics for nucleosynthesis in collapsars. *The Astrophysical Journal*, 902(1):66, 2020.
- Ohana, R., McCabe, M., Meyer, L., Morel, R., Agocs, F. J., Beneitez, M., Berger, M., Burkhart, B., Burns, K., Dalziel, S. B., Fielding, D. B., Fortunato, D., Goldberg, J. A., Hirashima, K., Jiang, Y.-F., Kerswell, R. R., Maddu, S., Miller, J., Mukhopadhyay, P., Nixon, S. S., Shen, J., Wateaux, R., Blancard, B. R.-S., Rozet, F., Parker, L. H., Cranmer, M., and Ho, S. The well: a large-scale collection of diverse physics simulations for machine learning, 2025. URL <https://arxiv.org/abs/2412.00568>.
- Pant, P., Doshi, R., Bahl, P., and Barati Farimani, A. Deep learning for reduced order modelling and efficient temporal evolution of fluid simulations. *Physics of Fluids*, 33(10):107101, 10 2021. ISSN 1070-6631. doi: 10.1063/5.0062546. URL <https://doi.org/10.1063/5.0062546>.
- Ronneberger, O., Fischer, P., and Brox, T. U-net: Convolutional networks for biomedical image segmentation, 2015. URL <https://arxiv.org/abs/1505.04597>.
- Ruiz, R. B., Marwah, T., Gu, A., and Risteski, A. On the benefits of memory for modeling time-dependent pdes, 2025. URL <https://arxiv.org/abs/2409.02313>.
- Subramanian, S., Harrington, P., Keutzer, K., Bhimji, W., Morozov, D., Mahoney, M., and Gholami, A. Towards foundation models for scientific machine learning: Characterizing scaling and transfer behavior, 2023. URL <https://arxiv.org/abs/2306.00258>.
- Takamoto, M., Praditia, T., Leiteritz, R., MacKinlay, D., Alesiani, F., Pflüger, D., and Niepert, M. Pdebench: An extensive benchmark for scientific machine learning, 2024. URL <https://arxiv.org/abs/2210.07182>.
- Wen, S., Kumbhat, A., Lingsch, L., Mousavi, S., Zhao, Y., Chandrashekar, P., and Mishra, S. Geometry aware operator transformer as an efficient and accurate neural surrogate for pdes on arbitrary domains, 2025. URL <https://arxiv.org/abs/2505.18781>.
- Wu, H., Luo, H., Wang, H., Wang, J., and Long, M. Transolver: A fast transformer solver for pdes on general geometries. *arXiv preprint arXiv:2402.02366*, 2024.
- Zakariaei, N., Rout, S., Haber, E., and Eliasof, M. Advection augmented convolutional neural networks, 2024. URL <https://arxiv.org/abs/2406.19253>.
- Zhu, X., Su, W., Lu, L., Li, B., Wang, X., and Dai, J. Deformable detr: Deformable transformers for end-to-end object detection. In *International Conference on Learning Representations (ICLR)*, 2021.
- Zhu, Y. and Zabaras, N. Bayesian deep convolutional encoder–decoder networks for surrogate modeling and uncertainty quantification. *Journal of Computational Physics*, 366:415–447, 2018. ISSN 0021-9991. doi: <https://doi.org/10.1016/j.jcp.2018.04.018>. URL <https://www.sciencedirect.com/science/article/pii/S0021999118302341>.

	FNO	CNEXTU-NET	SCOT	FLOWER
Optimal LR	1×10^{-3}	1×10^{-3}	5×10^{-4}	1×10^{-3}
VRMSE	0.0987	0.1425	0.3068	0.0463

Table 4. Predictions on the 15Hz acoustic time-harmonic Helmholtz equation problem from WaveBench.

Map of Appendices

- Appendix A contains detailed information about the experiments, models and datasets, as well as additional experimental results, including the time-independent Helmholtz equation (wave speed to solution map) where FLOWER surprisingly performs well. It also compares the computational efficiency of FLOWERS to other architectures.
- Appendix B expands the discussion of the relationship between FLOWERS and conservation laws.
- Appendix D gives a detailed description of the FLOWER architecture.
- Appendix E derives the kinetic continuum limit of cascaded Flower blocks.
- Appendix F shows that geometric optics solutions to the linear wave equation naturally yield a multihead pullback structure.
- Appendix G describes related work on neural PDE solvers and neural operators.

A. Experiment Details

A.1. Benchmark Setup

In our experiments we generally follow the benchmark settings of The Well: we aim for a batch size utilizing above 90% of GPU memory (or the maximum possible otherwise), and limit training to 24 hours on a single NVIDIA H200 GPU (The Well uses 12 hours on an H100). This evaluates performance under a fixed wall-clock budget. As The Well contains datasets where simulation parameters varies across trajectory, we either need to provide these parameters directly to the model, or teach the model to infer them from a history of snapshots. We do the former in a 1-input-1-output setting, where the model receives simulation parameters as a separate tensor for use in conditioning FiLM layers. For the latter, we follow the benchmark setting of The Well, and provide 4 inputs to each model, stacked along the channel axis.

For the 4→1 setting depicted in Table 1, all models were tested on three different learning rates (1×10^{-3} , 5×10^{-4} , 1×10^{-4}) and the weights of the best validation VRMSE was selected. See Table 5 for the optimal learning rate per model and problem. For the 1→1 setting, where we give simulation parameters directly to the models, we ran a limited suite of experiments with a single learning rate per model, with the results depicted in Table 7.

A.2. Models

In this section we describe the models used for comparison. Following the experimental setup of the The Well benchmark, we scale all models to between 15 and 20 million parameters for 2D problems. We naturally extend these models to 3D (as is done in The Well), which leads to modest increases in parameter size for the CNUNET (approx. 22M parameters) and FLOWER (approx. 24M parameters), but causes the FNO to reach almost 300M parameters. As SCOT does not support 3D-data, we omit it from 3D benchmarks.

We train all models using AdamW (Loshchilov & Hutter, 2019) and a linear warm up of the learning rate over 5 epochs, followed by cosine decay. All models were trained for 100 epochs or until 24 hours of training time on an H200 GPU, whichever came first. This time constraint intentionally biases our comparison toward more efficient models and follows the spirit of The Well’s benchmark setup. Model-specific hyperparameters (learning rate and weight decay) were set according to their respective original papers, with details provided in the following subsection.

A.2.1. FNO

We employ a standard FNO architecture consisting of three main components: an initial lifting layer that projects inputs to a high-dimensional latent space, a series of FNO blocks that perform spectral convolutions, and a final projection layer that maps back to the desired number of output channels.

Collection	Dataset	FNO	CNUNET	SCOT	FLOWER
The Well	acoustic_scattering_maze	1×10^{-3}	1×10^{-3}	1×10^{-3}	1×10^{-3}
	active_matter	1×10^{-3}	1×10^{-3}	1×10^{-3}	1×10^{-3}
	gray_scott_reaction_diffusion	5×10^{-4}	1×10^{-4}	1×10^{-3}	5×10^{-4}
	MHD_64	1×10^{-3}	1×10^{-3}	–	5×10^{-4}
	planetswe	1×10^{-4}	1×10^{-4}	1×10^{-3}	5×10^{-4}
	post_neutron_star_merger	5×10^{-4}	1×10^{-3}	–	5×10^{-4}
	rayleigh_benard	1×10^{-4}	1×10^{-3}	5×10^{-4}	1×10^{-3}
	rayleigh_taylor_instability	5×10^{-4}	5×10^{-4}	–	1×10^{-3}
	shear_flow	5×10^{-4}	1×10^{-4}	1×10^{-3}	5×10^{-4}
	supernova_explosion_128	1×10^{-3}	5×10^{-4}	–	1×10^{-3}
	turbulence_gravity_cooling	5×10^{-4}	5×10^{-4}	–	5×10^{-4}
	turbulent_radiative_layer_2D	1×10^{-3}	5×10^{-4}	1×10^{-3}	1×10^{-3}
	turbulent_radiative_layer_3D	1×10^{-3}	1×10^{-4}	–	1×10^{-3}
	viscoelastic_instability	1×10^{-3}	5×10^{-4}	5×10^{-4}	1×10^{-3}
PDEBench	diffusion_reaction	1×10^{-4}	5×10^{-4}	1×10^{-3}	1×10^{-3}
	shallow_water	1×10^{-3}	5×10^{-4}	1×10^{-3}	1×10^{-3}

Table 5. Best learning rate $4 \rightarrow 1$ next-step prediction.

Following the `neuralops` (Kossaifi et al., 2024; Kovachki et al., 2021) implementation, we use a local 2-layer MLP for both the lifting and projection operations. The lifting layer employs an inverted bottleneck structure, where the hidden dimension of the MLP is $2 \times$ the latent dimension. Similarly, each FNO block follows the `neuralops` architecture, with one exception: we insert an InstanceNorm layer before the non-linearity, which we expand to a FiLM layer in case of conditioning. Specifically, each block performs a spectral convolution restricted to low-frequency modes in parallel with a local linear skip connection. The outputs of these two operations are summed and passed through the normalization layer, then through a GELU activation function. Following POSEIDON’s (Herde et al., 2024) FNO implementation, we use InstanceNorm rather than alternatives such as GroupNorm or LayerNorm.

As input, we concatenate the initial field with a positional grid and the conditioning information. We choose a lifting dimension of 180, 16 fourier modes and use 4 blocks, resulting in a total of approximately 18,929,704 parameters.

In The Well benchmark, the median optimal learning rate for the FNO was 1×10^{-3} , which we adopt here. We also copy the weight decay of 1×10^{-2} .

A.2.2. CNEXTU-NET

We use the CNextU-Net architecture as described in the Well benchmark, with one modification: when conditioning is applied, we replace the standard LayerNorm in each ConvNeXt block with a FiLM LayerNorm layer. As input, we concatenate the initial field with the conditioning information. We adopt the hyperparameters specified in the Well benchmark, resulting in a model with approximately 18,570,807 parameters.

In The Well benchmark, the median optimal learning rate for the CNextU-Net was 1×10^{-3} , which we adopt here. We also copy the weight decay of 1×10^{-2} .

A.2.3. SCOT

We include `scOT` (Herde et al., 2024) for comparison with an attention-based method. While the original `scOT` implementation expects square 2D domains, we extend the model to handle rectangular 2D domains. Since `scOT` already employs time-conditioned LayerNorm layers for lead-time prediction, we repurpose these for general conditioning.

We configure the model with a patch size of 4, embedding dimension of 32, depths of [8, 8, 8, 8], attention heads of [2, 4, 8, 16], one residual block per skip connection stage, window size of 7, and MLP ratio of 4.0, yielding a model with approximately 17,779,868 parameters.

We use a learning rate of 5×10^{-4} and weight decay of 1×10^{-6} as reported in the original paper (Herde et al., 2024).

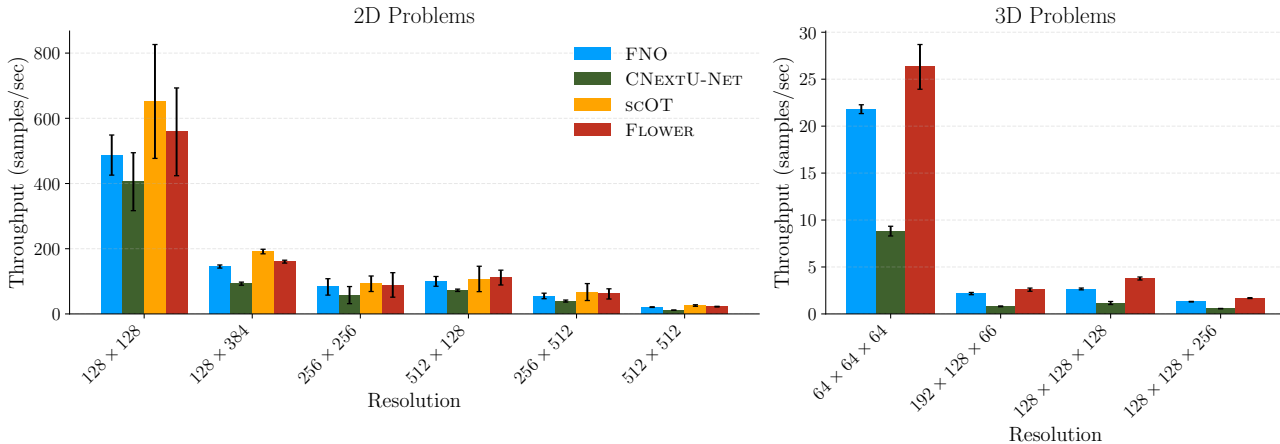


Figure 7. Comparison of model throughput (samples/sec) across resolutions for 2D and 3D problems, measured during the training runs of Table 1. Throughput is calculated as batch size divided by time per batch and includes both forward and backward passes. Error bars indicate standard deviation across datasets.

	FNO	CNUNET	SCOT	FLOWER
VRMSE	0.0987	0.1425	0.3068	0.0463

Table 6. Results on WaveBench `helmholtz_anisotropic`. Best learning rates: FNO 1×10^{-3} , CNextU-net 1×10^{-3} , scOT 5×10^{-4} , FLOWER 1×10^{-3} .

A.2.4. FLOWER

For a detailed description of the architecture we refer to Section 2 and in particular Appendix D.

FLOWER, as used in the benchmark setting, has an initial lift to 160 channels, and 4 levels encoding/decoding. We choose 40 heads and set the number of GroupNorm groups to 40. This model has approximately 17,329,362 parameters.

For our scaling analysis, we constructed versions of this model with increased channel and head numbers, scaled in proportion. FLOWER-S has an initial lift to 320 channels with 80 heads, giving approximately 69,274,725 parameters and FLOWER-M lifts to 480 channels with 120 heads, giving approximately 155,828,885 parameters.

A.3. Datasets

We adapt the codebase from The Well (Ohana et al., 2025) and use most datasets (Mandli et al., 2016; Maddu et al., 2024; Burkhart et al., 2020; McCabe et al., 2023; Miller et al., 2019a;b; 2020; Curtis et al., 2023; Lund et al., 2024; Burns et al., 2020; Hirashima et al., 2023a;b; Fielding et al., 2020) as they are. The exception is the viscoelastic instability (Beneitez et al., 2024) dataset, which erroneously contained duplicate frames that we removed. This improves the performance of every model.

Our results on other datasets may differ from The Well’s published scores due to a bug in the original benchmark code. Once corrected, we expect the results to align.

We also tested our model on two datasets from PDEBench (Takamoto et al., 2024) and a time-independent Helmholtz problem from WaveBench (Liu et al., 2024). We included the latter as an expected failure case: we did not anticipate FLOWER to perform well on this problem. Surprisingly, it does, and we do not yet fully understand why.

A.4. More Results

B. Motivation via Conservation Laws

FLOWERS achieve excellent performance on forecasting solutions to nonlinear systems of conservation laws. In this

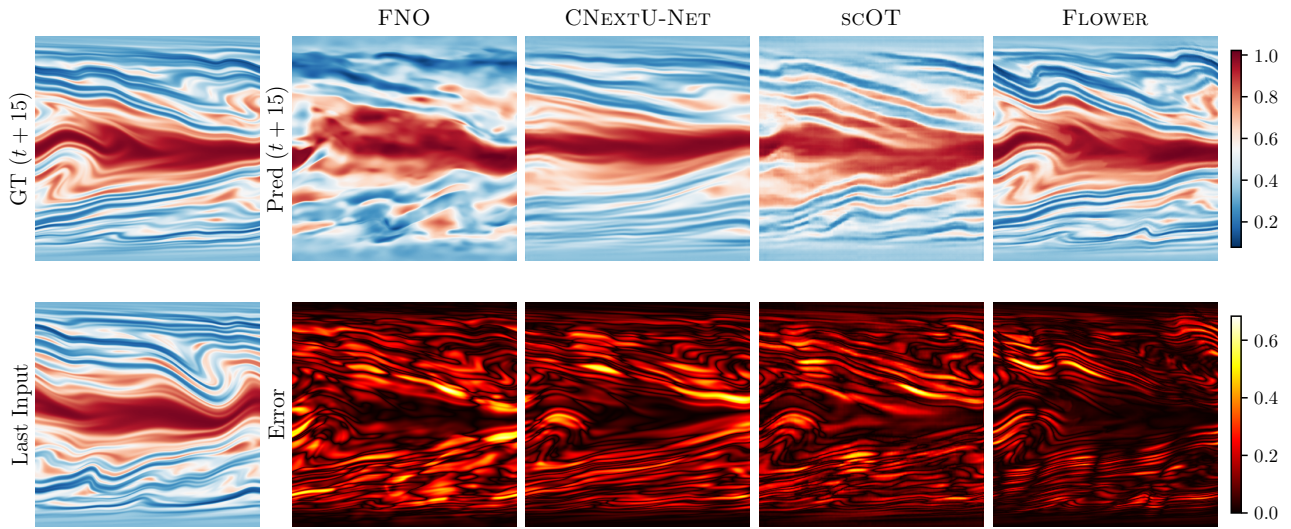


Figure 8. Comparison of autoregressive model predictions on the viscoelastic instability dataset (4→1 unconditioned setting), showing the conformation tensor entry C_{zz} . The top row shows the ground truth and the prediction of each model, bottom row shows the last of the four input frames and prediction errors.

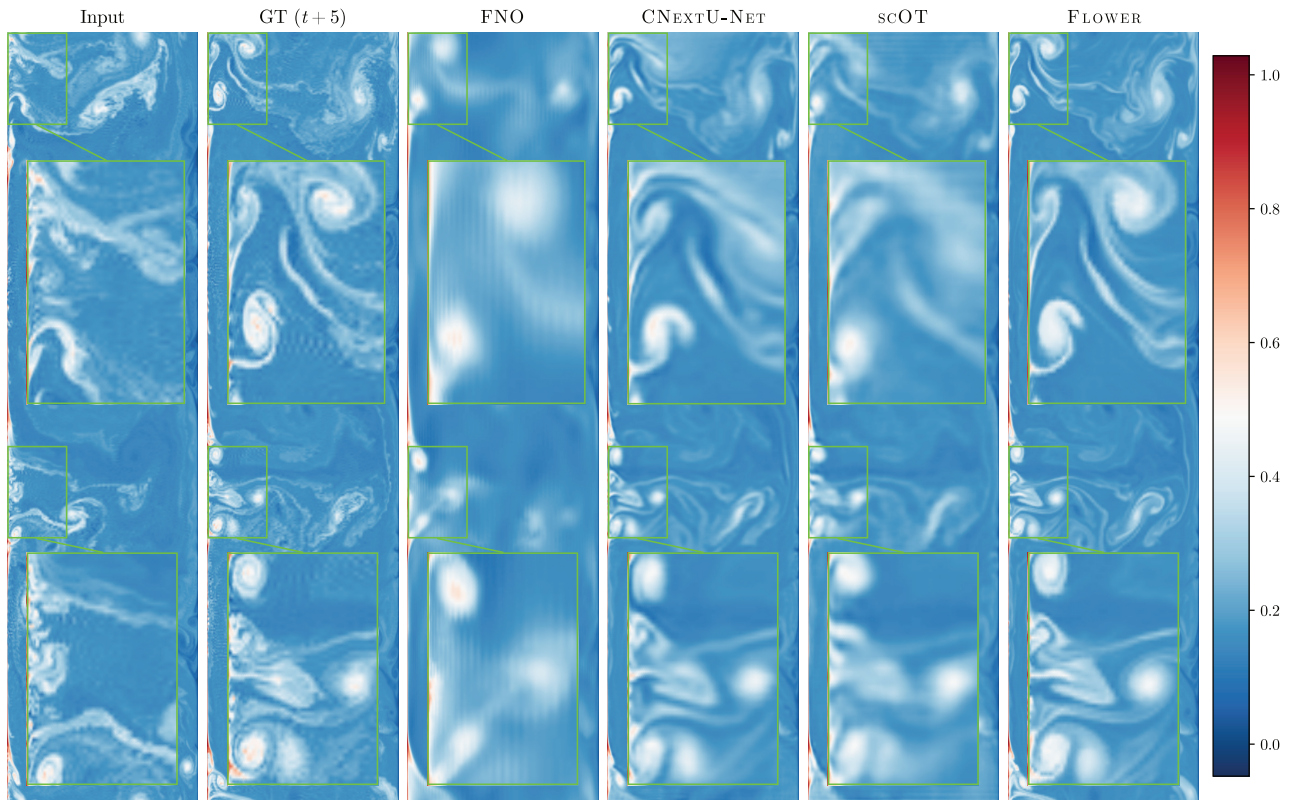


Figure 9. Comparison of model predictions on the Rayleigh-Bénard dataset (4→1 unconditioned setting), showing the buoyancy. We use blow-outs to enhance regions of interest.

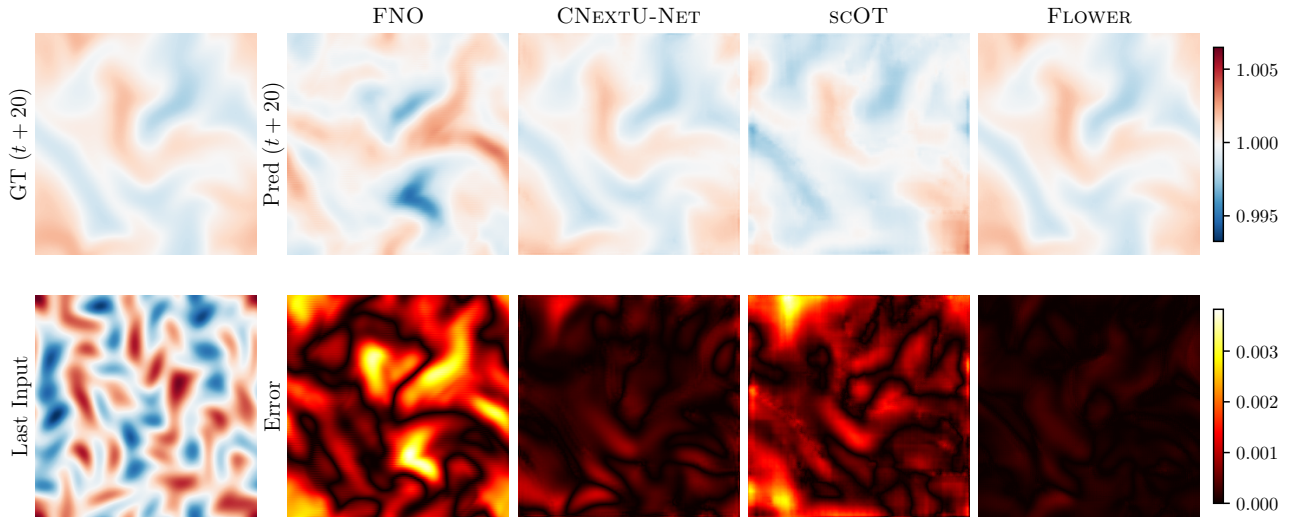


Figure 10. Comparison of autoregressive model predictions on the active matter dataset ($4 \rightarrow 1$ unconditioned setting), showing the concentration. The top row shows the ground truth and the prediction of each model, bottom row shows the last of the four input frames and prediction errors.

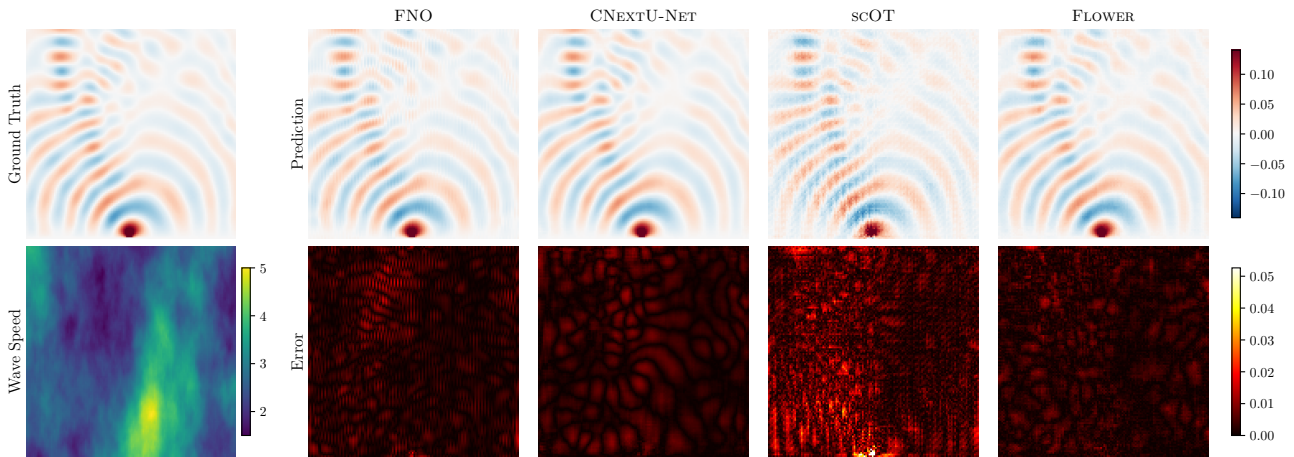


Figure 11. Comparison of model predictions on WaveBench's helmholtz_anisotropic 15Hz dataset. The top row shows the ground truth and the prediction of each model, bottom row shows the input (background wavespeed) and prediction errors.

Collection	Dataset	FNO	CNEXTU-NET	SCOT	FLOWER
The Well	acoustic_scattering (maze)	0.1650	0.0126	0.0378	0.0077
	active_matter	0.2200	0.0918	0.1934	0.0397
	MHD_64	0.3543	0.1895	–	0.1378
	planetswe	0.0255	0.0041	0.0050	0.0018
	rayleigh_benard	0.2589	0.1395	0.2295	0.0706
	shear_flow	0.0791	0.0650	0.1383	0.0285
	supernova_explosion_128	0.5911	0.5038	–	0.3440
turbulent_radiative_layer_2D	0.3326	0.2652	0.3823	0.1907	

Table 7. VRMSE loss for conditioned 1→1 next-step prediction. Best results marked in bold. We did not test multiple learning rates in this setting, instead all models trained with a learning rate of 1×10^{-3} , except SCOT where 5×10^{-4} was used, as reported in the original paper (Herde et al., 2024).

	FNO	CUNET	SCOT	FLOWER	FLOWER (single-scale)
Next-step VRMSE	0.2104	0.2171	0.1863	0.0807	0.1565
1:20 Rollout VRMSE	39.038	12.507	5.6486	2.1661	2.8323

Table 8. Results for a single-scale FLOWER variant on rayleigh_benard. The model embeds inputs into 16×16 patches and processes them at fixed resolution until de-embedding, rather than using the U-net multiscale structure. Since channel counts remain constant, IdProj is unnecessary; we reallocate this convolution to a projection after the warp and rearrange operations for best performance, giving: $u \mapsto u + \phi \circ \text{Proj} \circ \text{Warp}_{V,g} \circ \text{Norm}[u]$. Other model’s results are taken from Table 1 and added for comparison.

appendix we motivate the main primitive—a local pullback, or warping—using a simple scalar conservation law. Our goal is to build intuition, and the theory for systems is far more complicated.

In this appendix, we show that short time solutions of the scalar conservation laws can be approximated using a single layer warping network. On long time intervals the shocks can appear in the solutions of the conservation laws and hence the classical solutions may not exist. However, one can define generalized viscosity solutions that exist beyond the appearance of shocks.

We consider $x \in \mathbb{R}^d$. The relevant equation is

$$\begin{cases} \partial_t u(t, x) + \nabla_x \cdot (G(u(t, x))) = 0, & u(0, x) = u^0(x), \\ u : \mathbb{R}_+ \times \mathbb{R}^d \rightarrow \mathbb{R}, & G : \mathbb{R} \rightarrow \mathbb{R}^d. \end{cases} \quad (4)$$

We write this as a nonlinear optical flow

$$\begin{cases} \partial_t u(t, x) + A(u(t, x)) \cdot \nabla_x u(t, x) = 0, & u(0, x) = u^0(x), \\ u : \mathbb{R}_+ \times \mathbb{R}^d \rightarrow \mathbb{R}^d, & A : \mathbb{R}^d \rightarrow \mathbb{R}^d, \end{cases} \quad (5)$$

where

$$A(u) = \frac{d}{du} G(u).$$

A generalization would be to let A explicitly depend on t and x but we do not consider this here.

As a point of departure, characteristics are given by

$$\frac{d}{dt} \Phi_t(x) = A(u(t, \Phi_t(x))), \quad \Phi_0(x) = x. \quad (6)$$

Solutions of (5) are constant along characteristic curves $t \rightarrow (t, \Phi_t(x))$. Indeed, substituting $u(t, \Phi_t(x))$ into equation (5),

$$\begin{aligned} \partial_t u(t, \Phi_t(x)) &= [\partial_t u(t, z)]_{z=\Phi_t(x)} + [\nabla_z u(t, z)]_{z=\Phi_t(x)} \cdot \partial_t \Phi_t(x) \\ &= [\partial_t u(t, z)]_{z=\Phi_t(x)} + [\nabla_z u(t, z)]_{z=\Phi_t(x)} \cdot [A(u(t, z))]_{z=\Phi_t(x)} \\ &= [\partial_t u(t, z) + A(u(t, z)) \cdot \nabla_z u(t, z)]_{z=\Phi_t(x)} \\ &= 0 \end{aligned} \quad (7)$$

and thus we see that

$$\frac{d}{dt}u(t, \Phi_t(x)) = 0$$

so that

$$u(t, \Phi_t(x)) = u^0(x). \quad (8)$$

Substituting (8) into (6), we find that the characteristics depend on $u(t, x)$ only through the initial condition $u_0(x)$:

$$\frac{d}{dt}\Phi_t(x) = A(u^0(x)), \quad \Phi_0(x) = x. \quad (9)$$

As $\Phi_t(x)$ depends only on $u^0(x)$ (that is, not on values of $u^0(x')$ at points $x' \neq x$), we write it as

$$\Phi_t(x) = \Phi_t^{u^0(x)}(x), \quad (10)$$

and moreover,

$$\Phi_t(x) = \Phi_t^{u^0(x)}(x) = x + tA(u^0(x)). \quad (11)$$

This shows that (8) is equivalent to

$$u(t, x + tA(u^0(x))) = u^0(x). \quad (12)$$

Consider the case where $t > 0$ is so small that $t \cdot \text{Lip}(A(u_0(\cdot))) < 1$. Then, by Banach fixed point theorem, the function $F_t : x \rightarrow x + tA(u^0(x))$ is invertible. Let $G_t = F_t^{-1} : \mathbb{R}^d \rightarrow \mathbb{R}^d$ be the inverse function of $F_t : \mathbb{R}^d \rightarrow \mathbb{R}^d$.

Up to this point our discussion has been precise. In what follows we will discuss, somewhat non-rigorously, why FLOWERS can be used to approximate the function G_t .

Let $B = A \circ u^0 : \mathbb{R}^d \rightarrow \mathbb{R}^d$. Below, we assume that B is $C^3(\mathbb{R}^d)$. By using (11), we see that G_t satisfies the equation

$$G_t(x) = x - tB(G_t(x)).$$

Then,

$$u(t, x) = u^0(G_t(x)). \quad (13)$$

Let us consider the Taylor expansion of $G_t(x)$ in variable t around the time zero,

$$G_t(x) = x + tg_1(x) + t^2g_2(x) + O(t^3).$$

By operating on both sides of this equation with B and using Taylor-expansion around x ,

$$B(y) = B(x) + B'(x)(y - x) + O(|y - x|^2), \quad B'(x) = DB(x) \in \mathbb{R}^{d \times d},$$

we obtain

$$B(G_t(x)) = B(x + tg_1(x) + t^2g_2(x)) = B(x) + tB'(x)g_1(x) + O(t^2).$$

Hence,

$$x + tg_1(x) + t^2g_2(x) = x - t(B(x) + tB'(x)g_1(x) + O(t^2)) = x - tB(x) - t^2B'(x)g_1(x) + O(t^3).$$

Matching coefficients we get

$$g_1(x) = -B(x) = -A(u^0(x)), \quad g_2(x) = B'(x)B(x).$$

Combining the above formulas, we obtain

$$\begin{aligned} G_t(x) &= x - tB(x) + t^2B'(x)B(x) + O(t^3) \\ &= x - tA(u^0(x)) + t^2D[A \circ u^0](x)A(u^0(x)) + O(t^3), \end{aligned}$$

where by the chain rule, the Jacobian matrix $DB(x) = D[A \circ u^0](x)$ is given by

$$D[A \circ u^0](x) = A'(u^0(x))(\nabla u^0(x))^\top,$$

where A' is the derivative of the map of the map $A : \mathbb{R} \rightarrow \mathbb{R}^d$. Thus the 1st order approximation of $G_t(x)$ in t is

$$G_t(x) \approx x - tA(u^0(x))$$

which defines a pointwise-dependent displacement map considered below in Section D.1. The 2nd order approximation of $G_t(x)$ in t is given by

$$G_t(x) \approx x - tA(u^0(x)) + t^2 A'(u^0(x))(\nabla u^0(x))^\top A(u^0(x))$$

Here, the derivative $\nabla u^0(x)$ can be approximated using a multi-head warp network (see Section D.1 below) as $\nabla u^0(x)^\top = (\frac{\partial}{\partial x^1} u^0(x), \dots, \frac{\partial}{\partial x^d} u^0(x))$ can be approximated by

$$\frac{\partial}{\partial x^j} u^0(x) = \frac{1}{s} \left(\begin{array}{c} (Id + \varrho_{j,s})^* \\ -Id \end{array} \right)^\top \begin{pmatrix} u^0(x) \\ u^0(x) \end{pmatrix} + O(s),$$

where $\varrho_{j,s}(x) = se_j$, $s > 0$ is small, and $e_j = (0, 0, \dots, 0, 1, 0, \dots, 0)$ are the unit coordinate vectors.

C. Approximation of convolution integral operators by pullback networks

We show that convolutions can be recovered as a special (non-adaptive) case of our modules. This capability may be useful for non-hyperbolic physics, for example to implement the divergence-free projections or diffusion. We start from a simplified model where the shift $m(x; h)$ is independent of x , that is, $m(x; h) = m(h)$. For each head $h \in \mathbb{R}^k$ and input function f , we denote

$$f_h(x) = f(x + m(h)) = ((Id + m(h))^* f)(x)$$

Let us add weights $k(x, h)$ (or value matrices) that depend on variable x and integrate (or sum) over the head variable. This gives us operators,

$$A_{k,m} f(x) = \int_{\mathbb{R}^d} k(x, h) f(x + m(h)) dh.$$

Assume now that $m(h) = -h$. By introducing a new variable $y = x - h$ we obtain

$$\begin{aligned} A_{k,m} f(x) &= \int_{\mathbb{R}^d} k(x, h) f(x - h) dh \\ &= \int_{\mathbb{R}^d} k(x, x - y) f(y) dy. \end{aligned}$$

This shows that the operators $A_{k,m}$ can be an arbitrary linear integral operator with kernel $k(x, x - y)$. Thus, one can approximate any convolution integral operator by pullback networks.

If the weights $k(x, h)$ are independent of x , that is, $k(x, h) = k(h)$ the operators $A_{k,m}$ can be arbitrary convolution operators.

D. A detailed description of the architecture

For clarity we describe the pullback layer over continuous coordinates; in practice the pullback is implemented by differentiable interpolation on a grid with a boundary extension determined by the chosen boundary conditions.

D.1. Feature spaces and notation conventions

Let $\Omega \subset \mathbb{R}^d$ be the spatial domain, $\mathcal{F}(\Omega)$ a sufficiently rich space of real-valued functions on Ω , and

$$\mathcal{F}^C := \{u : \Omega \rightarrow \mathbb{R}^C\}$$

the space of fields with C channels.

We write u, v, w for fields, $x \in \Omega$ for spatial coordinates, and $a = u(x) \in \mathbb{R}^C$ for pointwise channel vectors. Operators acting on fields take arguments in brackets (e.g. $A[u]$); finite-dimensional maps take arguments in parentheses (e.g. $g(a), \tau(x)$).

Broadcast Given a local map $h : \mathbb{R}^p \rightarrow \mathbb{R}^q$, its broadcast (pointwise) extension is

$$h[\cdot] : \mathcal{F}^p(\Omega) \rightarrow \mathcal{F}^q(\Omega), \quad (h[u])(x) := h(u(x)).$$

Concatenation For $u \in \mathcal{F}^{C_1}(\Omega)$ and $v \in \mathcal{F}^{C_2}(\Omega)$, we define channel concatenation as

$$u \oplus v \in \mathcal{F}^{C_1+C_2}(\Omega), \quad (u \oplus v)(x) = u(x) \oplus v(x) = [u_1(x), \dots, u_{C_1}(x), v_1(x), \dots, v_{C_2}(x)].$$

Pullback Given a map $\tau : \Omega \rightarrow \mathbb{R}^d$, define the associated pullback operator

$$\tau^* : \mathcal{F}^C(\Omega) \rightarrow \mathcal{F}^C(\Omega), \quad (\tau^*v)(x) := v(\tau(x)).$$

For a displacement field $\varrho \in \mathcal{F}^d(\Omega)$ we write $\tau = \text{Id} + \varrho : \Omega \rightarrow \mathbb{R}^d$ for the map $x \mapsto x + \varrho(x)$.

D.2. Multihead (pullback / spatial warp)

Fix integers $C_{\text{in}}, C_{\text{out}} \geq 1$ and a head count $H \geq 1$ with $C_{\text{out}} = HC_h$. A multihead pullback layer is determined by

- a local *value* projection $f : \mathbb{R}^{C_{\text{in}}} \rightarrow \mathbb{R}^{C_{\text{out}}}$ of the form $f(a) = Va$, where V is a matrix;
- a local *multihead displacement* map $g : \mathbb{R}^{C_{\text{in}}} \rightarrow (\mathbb{R}^d)^H$ with components $g^{(h)} : \mathbb{R}^{C_{\text{in}}} \rightarrow \mathbb{R}^d$. (In the code, g is a small pointwise MLP realized by 1×1 convolutions.)

We will now define the key building block operator

$$\text{Warp}_{V,g} : \mathcal{F}^{C_{\text{in}}}(\Omega) \rightarrow \mathcal{F}^{C_{\text{out}}}(\Omega).$$

For $u \in \mathcal{F}^{C_{\text{in}}}(\Omega)$ set

$$v := f[u] \in \mathcal{F}^{C_{\text{out}}}(\Omega), \quad [\varrho^{(1)}, \dots, \varrho^{(H)}] := g[u] \in (\mathcal{F}^d(\Omega))^H,$$

split $v = v^{(1)} \oplus \dots \oplus v^{(H)}$ with $v^{(h)} \in \mathcal{F}^{C_h}(\Omega)$, and define head warps $\tau_u^{(h)} := \text{Id} + \varrho^{(h)}$. Then

$$\text{Warp}_{V,g}[u] = \bigoplus_{h=1}^H (\tau_u^{(h)})^* v^{(h)} = \bigoplus_{h=1}^H (\text{Id} + g^{(h)}[u])^* (f^{(h)}[u]).$$

For $H = 1$ this reduces to the single-head layer $u \mapsto (\text{Id} + g[u])^*(Vu)$.

D.3. Residual pullback block (FlowerBlock)

Fix the number of input and output channels $C_{\text{in}}, C_{\text{out}}$. A *FlowerBlock* is an operator

$$\text{Block} : \mathcal{F}^{C_{\text{in}}}(\Omega) \rightarrow \mathcal{F}^{C_{\text{out}}}(\Omega),$$

defined by

$$\text{Block} = \phi \circ \text{Norm} \circ \left(\text{Warp}_{V,g} + \text{IdProj} \right).$$

Here $\text{IdProj} : \mathcal{F}^{C_{\text{in}}}(\Omega) \rightarrow \mathcal{F}^{C_{\text{out}}}(\Omega)$ is a pointwise linear projection (a 1×1 convolution) and ϕ is a pointwise nonlinearity (GELU). Norm is group normalization.²

²For conditioned prediction we use FiLM modulated normalization.

D.4. Multiscale (U-Net) Flowers

We arrange FlowerBlocks into a U-Net with L levels. Let Ω_0 denote the finest-resolution domain (in practice a grid), and let $\Omega_{\ell+1}$ be obtained from Ω_ℓ by downsampling by a factor of 2 in each spatial direction. Define channel widths

$$c_0 := c_{\text{lift}}, \quad c_\ell := 2^\ell c_0, \quad \ell = 0, \dots, L-1.$$

Positional augmentation and lifting Let $\xi \in \mathcal{F}^d(\Omega_0)$ be the coordinate field (positional grid) so that $\xi(x) = x$. Define the augmentation operator

$$\text{Aug} : \mathcal{F}^{C_{\text{in}}}(\Omega_0) \rightarrow \mathcal{F}^{C_{\text{in}}+d}(\Omega_0), \quad \text{Aug}[u] := u \oplus \xi,$$

and a pointwise lifting map

$$\text{Lift} : \mathcal{F}^{C_{\text{in}}+d}(\Omega_0) \rightarrow \mathcal{F}^{c_0}(\Omega_0).$$

Encoder-side operators For $\ell = 0, \dots, L-2$, let

$$E_\ell : \mathcal{F}^{c_\ell}(\Omega_\ell) \rightarrow \mathcal{F}^{c_{\ell+1}}(\Omega_{\ell+1})$$

denote the encoder stage

$$E_\ell = \rho \circ \text{DownConv}_\ell \circ \text{Block}_\ell^\downarrow,$$

where $\text{Block}_\ell^\downarrow : \mathcal{F}^{c_\ell}(\Omega_\ell) \rightarrow \mathcal{F}^{c_\ell}(\Omega_\ell)$ is a FlowerBlock (same in/out channels), DownConv_ℓ is a stride-2 convolution mapping $c_\ell \mapsto c_{\ell+1}$, and ρ is ReLU.

Bottleneck Let

$$\text{Bot} : \mathcal{F}^{c_{L-1}}(\Omega_{L-1}) \rightarrow \mathcal{F}^{c_{L-1}}(\Omega_{L-1})$$

be a FlowerBlock at the coarsest scale.

Decoder-side operators Define decoder channel sizes

$$\tilde{c}_{L-1} := c_{L-1}, \quad \tilde{c}_\ell := 2c_\ell \quad (\ell = 0, \dots, L-2),$$

so that after concatenating a skip at level ℓ the decoder state has $2c_\ell$ channels. For $\ell = 1, \dots, L-1$, define an up stage

$$U_\ell : \mathcal{F}^{\tilde{c}_\ell}(\Omega_\ell) \rightarrow \mathcal{F}^{c_{\ell-1}}(\Omega_{\ell-1})$$

by

$$U_\ell = \rho \circ \text{UpConv}_\ell \circ \text{Block}_\ell^\uparrow,$$

where $\text{Block}_\ell^\uparrow : \mathcal{F}^{\tilde{c}_\ell}(\Omega_\ell) \rightarrow \mathcal{F}^{c_{\ell-1}}(\Omega_\ell)$ is a FlowerBlock that reduces channels, UpConv_ℓ is a stride-2 transposed convolution preserving channel count $c_{\ell-1}$ while upsampling $\Omega_\ell \rightarrow \Omega_{\ell-1}$, and ρ is ReLU.

Final projection Let

$$\text{Proj} : \mathcal{F}^{2c_0}(\Omega_0) \rightarrow \mathcal{F}^{C_{\text{out}}}(\Omega_0)$$

be the pointwise projection

$$\text{Proj} = W_2 \circ \rho \circ W_1,$$

where W_1 maps $2c_0 \mapsto c_0$ and W_2 maps $c_0 \mapsto C_{\text{out}}$ (both 1×1 convolutions), and ρ is ReLU.

Definition (Flower) The full network is an operator

$$\Phi : \mathcal{F}^{C_{\text{in}}}(\Omega_0) \rightarrow \mathcal{F}^{C_{\text{out}}}(\Omega_0),$$

defined by the recursion

$$\begin{aligned} x_0 &:= \text{Lift}(\text{Aug}[u]), \\ \text{for } \ell = 0, \dots, L-2 : \quad s_\ell &:= x_\ell, \quad x_{\ell+1} := E_\ell[x_\ell], \\ d_{L-1} &:= \text{Bot}[x_{L-1}], \\ \text{for } \ell = L-1, \dots, 1 : \quad \hat{d}_{\ell-1} &:= U_\ell[d_\ell], \quad d_{\ell-1} := \hat{d}_{\ell-1} \oplus s_{\ell-1}, \end{aligned}$$

and finally

$$\Phi[u] = \text{Proj}[d_0].$$

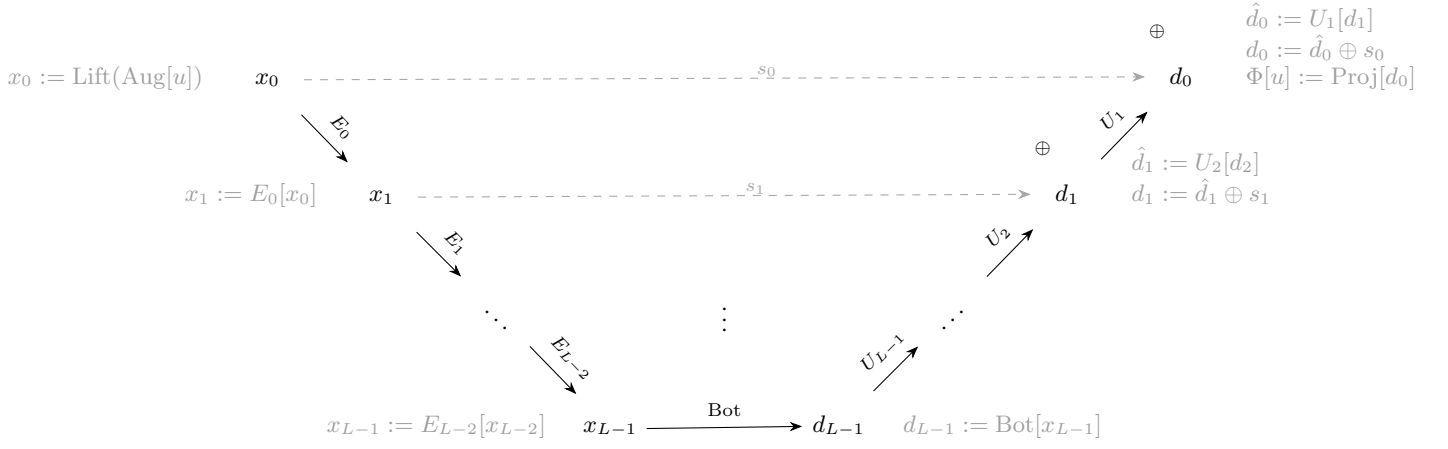


Figure 12. A schematic illustration of the FLOWER U-Net architecture.

E. The continuum limit and kinetic theory perspective

We use similar notation as in Appendix D but work with a single-scale architecture, without the U-Net. In particular, let H be the number of heads and write (moving the head index to the argument)

$$u(x) = (u(x, 1), \dots, u(x, H)), \quad \text{with } u(x, h) \in \mathbb{R}^c,$$

so that $u \in \mathcal{F}^{Hc}(\Omega)$ and $u(x) \in \mathbb{R}^{Hc}$. A multihead warp has two pointwise components,

- a value map $V : \mathbb{R}^{Hc} \rightarrow \mathbb{R}^{Hc}$ (a 1×1 linear (affine) convolution mixing channels and heads; here we assume that we are already “in the lift” and the number of channels is constant so that we can derive a meaningful limit;
- a displacement map $g : \mathbb{R}^{Hc} \rightarrow (\mathbb{R}^d)^H$ with head components $g^{(h)} : \mathbb{R}^{Hc} \rightarrow \mathbb{R}^d$; this a pointwise MLP (implemented via a convnet with 1×1 convolutions).

For a $u \in \mathcal{F}^{Hc}(\Omega)$, let $v := V[u]$ and $\varrho^{(h)} = g^{(h)}[u]$. Define the warped outputs for each head as

$$(\text{Warp}_{V,g}[u])(x, h) := (\text{Id} + \varrho^{(h)})^* v(\cdot, h)(x) = v(x + \varrho^{(h)}(x), h).$$

Note that $x \mapsto \varrho^{(h)}(x)$ only depends on $u(x)$; non-locality enters via the pullback.

We now interpret the discrete head index as a sampling of a continuous latent variable, $\eta \in \Lambda$ compact (which will turn out to have a kinetic interpretation). A mixing or integration over heads can then be viewed as an integration against some probability measure. Through a quadrature, with weights w_h and samples η_h , we identify

$$u(x, \eta_h) \text{ with } u(x, h).$$

Letting $H \rightarrow \infty$, we obtain a function $u \in \mathcal{F}^c(\Omega \times \Lambda)$ that can be interpreted as a kinetic field $u(x, \eta)$, that depends on positional variable $x \in \Omega$ and a directional (velocity) variable $\eta \in \Lambda$.

A Flower layer is (approximately) computing

$$\mathcal{A}(\text{Warp}_{V,g}[u] + P[u])$$

with P a pointwise linear map (a generalized skip connection) and \mathcal{A} a pointwise nonlinear map.³ We interpret this through the lens of kinetic theory: the pullback $x \mapsto \varrho(x, \eta)$ implements streaming in an η -dependent manner; the pointwise operations that mix channels and/or kinetic labels η at a fixed x implement interactions. Pointwise maps act along the kinetic variable, η , that is to say, on the functions $\eta \mapsto u(x, \eta)$ for each x .

³GroupNorm is not strictly local in space but we ignore this here as it is not a leading order effect. It anyway globally rescales the field.

Replacing layer index by time

By considering a probability measure μ on $\Lambda \subset \mathbb{R}^d$ and interpreting η_h to be the quadrature nodes $\eta_h \in \Lambda$ and corresponding weights $w_h \in \mathbb{R}$, $h = 1, \dots, H$, on the set Λ , we can consider sums over multiple heads as approximations of integrals over Λ obtained using a quadrature formula

$$\int_{\Lambda} F(\eta) d\mu(\eta) \approx \sum_{h=1}^H w_h F(\eta_h). \quad (14)$$

We consider a composition of $N + 1$ Flower blocks indexed by $n = 0, \dots, N$, let $\Delta t := T/N$, and write $t_n := n\Delta t$. We will interpret each layer as being “small” in the sense that we will assume that there are operators $\mathcal{B}_t(\eta; \cdot)$ and $\mathcal{Q}(\eta; \cdot)$ such that for each layer n ,

- the displacement function is given by

$$\varrho(x, \eta) = \Delta t \cdot \mathcal{B}_{t_n}(\eta; u_n(x, \cdot))$$

where

$$\mathcal{B}_{t_n}(\eta; u_n(x, \cdot)) = \sum_{h=1}^H b_{t_n}(\eta, \eta_h) u_n(x, \eta_h).$$

In several physical applications, see e.g. (18) below, the function $\mathcal{B}_{t_n}(\eta; u_n(x, \cdot))$ has the simple form, $\mathcal{B}_{t_n}(\eta; u_n(x, \cdot)) = \eta$;

- the local contribution of the layer is determined by

$$P[u] = \Delta t \cdot \mathcal{Q}_{t_n}(\eta; u_n(x, \cdot)),$$

where

$$\mathcal{Q}_{t_n}(\eta; u_n(x, \cdot)) = \sum_{h=1}^H q_{t_n}(\eta, \eta_h) u_n(x, \eta_h).$$

We then expand the pullback of u_n as

$$u_n(x + \Delta t \cdot \mathcal{B}_{t_n}(\eta; u_n(x, \cdot)), \eta) = u_n(x, \eta) + \Delta t \mathcal{B}_{t_n}(\eta; u_n(x, \cdot)) \cdot \nabla_x u_n(x, \eta) + O(\Delta t^2).$$

We get

$$u_{n+1}(x, \eta) = u_n(x, \eta) + \Delta t \mathcal{B}_{t_n}(\eta; u_n(x, \cdot)) \cdot \nabla_x u_n(x, \eta) + \Delta t \cdot \mathcal{Q}_{t_n}(\eta; u_n(x, \cdot)). \quad (15)$$

If

$$\mathcal{A} = I + \Delta t \cdot \mathcal{A}'$$

we can account for the composition with \mathcal{A} by redefining

$$\mathcal{B}_{t_n} := \mathcal{A}_{t_n} \mathcal{B}_{t_n}, \quad \mathcal{Q}_{t_n} := \mathcal{A}_{t_n} \mathcal{Q}_{t_n} + \mathcal{A}'_{t_n}. \quad (16)$$

With $t_n = n\Delta t$, through a finite difference approximation, assuming that as $N \rightarrow \infty$ and $\Delta t \rightarrow 0$ (and $\mathcal{A} \rightarrow I$), $u_n(t, x)$ converges to $u(t, x, \eta)$, we get the following PDE

$$\partial_t u(t, x, \eta) + \mathcal{B}_t(\eta; u(t, x, \cdot)) \cdot \nabla_x u(t, x, \eta) = \mathcal{Q}_t(\eta; u(t, x, \cdot)), \quad (17)$$

which is a nonlinear kinetic equation with a self-adaptive streaming velocity. A notable special case of this equation is

$$\partial_t u(t, x, \eta) + \eta \cdot \nabla_x u(t, x, \eta) = \mathcal{Q}_t(\eta; u(t, x, \cdot)), \quad (18)$$

which is the familiar Boltzmann equation upon interpreting u as a distribution of particles, and which is known to yield hydrodynamics by evaluating moments. The nonlinear equation (18) can be considered as a Boltzmann-like equation where the drift (the streaming velocity) depends on the local kinetic state (e.g. a distribution over microscopic velocities in the true Boltzmann case). This gives it a great deal of flexibility.

F. Linear waves

We consider the linear wave equation in \mathbb{R}^d , with a variable wave speed, $c = c(x)$,

$$\partial_t^2 u - c(x)^2 \Delta u = 0, \quad (t, x) \in [0, \infty) \times \mathbb{R}^d \quad (19)$$

with initial data $u(0, x) = u_0(x)$ and $\partial_t u(0, x) = u_1(x)$. Here, we focus on the three-dimensional case, that is, $d = 3$ on such times t that waves have not formed caustics, that is, the Riemannian geodesics associated to the travel time metric do not have conjugate points. We let $G(t, x; y)$ be the causal Green's function so that

$$u(t, x) = \int_{\mathbb{R}^d} \partial_t G(t, x; y) u_0(y) dy + \int_{\mathbb{R}^d} G(t, x; y) u_1(y) dy. \quad (20)$$

The derivation is standard, but we explicitly connect it with our architecture, FLOWERS. We use the geometric optics formalism. It states that for (relatively) small t and away from caustics, that is, focusing of wave fronts caused by lensing effects, $G(t, x; y)$ is concentrated on the wavefront surface $t = \tau(x; y)$, where $\tau(x; y)$ is the travel time or geodesic distance from the point y to the point x . This motivates the following ‘‘WKB Ansatz’’,

$$G(t, x; y) \approx A(x; y) \delta(t - \tau(x; y)), \quad (21)$$

where the amplitude coefficient A encodes the so-called geometric spreading. It can be shown that this ansatz (21) is correct ‘‘up to smooth terms’’. What this means is that it correctly propagates the high-frequency singularities.

Inserting the ansatz (21) into the wave equation (19) yields

$$A(1 - c(x)^2 |\nabla_x \tau|^2) \delta''(t - \tau) + c(x)^2 (2 \nabla_x A \cdot \nabla_x \tau + A \Delta_x \tau) \delta'(t - \tau) + \text{less singular terms} = 0.$$

To make G solve the wave equation (19) ‘‘up to less singular terms’’ away from $x = y$, we set the coefficients in front of the derivatives of the Dirac's delta distributions δ'' and δ' to zero (that is., we analyze the leading order wavefront singularities).

The δ'' coefficient yields the well-known eikonal equation for the travel times,

$$c(x)^2 |\nabla_x \tau(x; y)|^2 = 1, \quad \tau(y; y) = 0.$$

The δ' coefficient yields the transport equation which determines the geometric spreading $A(x; y)$,

$$2 \nabla_x A(x; y) \cdot \nabla_x \tau(x; y) + A(x; y) \Delta_x \tau(x; y) = 0.$$

For simplicity, we focus on the u_1 term (and assume that $u_0 \equiv 0$ for now). Using (21),

$$\int_{\mathbb{R}^d} G(t, x; y) u_1(y) dy \approx \int_{\mathbb{R}^d} A(x; y) \delta(t - \tau(x; y)) u_1(y) dy.$$

The delta function turns a volume integral into a surface integral over the surface $\{y : t(x; y) = t\}$:

$$\int_{\mathbb{R}^d} G(t, x; y) u_1(y) dy \approx \int_{t=\tau(x; y)} \frac{A(x; y)}{|\nabla_y \tau(x; y)|} u_1(y) dS(y).$$

The factor

$$W_1(x; y) := \frac{A(x; y)}{|\nabla_y \tau(x; y)|}$$

is a weight. The u_0 term would have the same structure, with a different weight, $W_0(x; y)$ say.

We can now make the pullback structure of the solution explicit. Before caustics form, the wavefront $\{y : \tau(x; y) = t\}$ can be parameterized by a ‘‘ray label’’ η , for example, the initial (tangent) direction on \mathbb{S}^{d-1} . Let $x(t, y, \eta)$ denote position of the ray at time t that emanated at the time 0 from the point $y \in \mathbb{R}^d$ to the direction $\eta \in \mathbb{S}^{d-1}$. The rays, that are equivalent to geodesic curves determined by the Riemannian metric $c(x)^{-2}(dx_1^2 + \dots + dx_d^2)$, are given by the ordinary differential equation,

$$\partial_t^2 x(t, y, \eta) = 2((\nabla \log c)(x(t, y, \eta)) \cdot \partial_t x(t, y, \eta)) \partial_t x(t, y, \eta) - c(x(t, y, \eta))^2 (\nabla \log c)(x(t, y, \eta)), \quad (22)$$

$$x(t, y, \eta)|_{t=0} = y, \quad \partial_t x(t, y, \eta)|_{t=0} = \eta. \quad (23)$$

In the absence of caustics, x , η and t determine uniquely y such that $x(t, y, \eta) = x$. We introduce the map, $\Gamma_{-t}(x, \eta) = y$. Then, under the change of variable $\eta \rightarrow \Gamma_{-t}(x, \eta)$, the surface measure on the surface $\{y \in \mathbb{R}^d : \tau(x; y) = t\}$ takes the form

$$\frac{dS(y)}{|\nabla_y \tau(x; y)|} = J(t, x, \eta) d\eta,$$

where J is the relevant Jacobian. Putting everything together, we now see that we can write (20) as an integral of pullbacks

$$u(t, x) \approx \int_{\mathbb{S}^{d-1}} W_0(t, x, \eta) u_0(\Gamma_{-t}(x, \eta)) J(t, x, \eta) d\eta + \int_{\mathbb{S}^{d-1}} W_1(t, x, \eta) u_1(\Gamma_{-t}(x, \eta)) J(t, x, \eta) d\eta,$$

signifying pullbacks of u_0 and u_1 for given t and η , or, upon introducing the ‘‘displacement’’, $\varrho(t, x, \eta) = \Gamma_{-t}(x, \eta) - x$,

$$u(t, x) \approx \int_{\mathbb{S}^{d-1}} W_0(t, x, \eta) u_0(x + \varrho(t, x, \eta)) J(t, x, \eta) d\eta + \int_{\mathbb{S}^{d-1}} W_1(t, x, \eta) u_1(x + \varrho(t, x, \eta)) J(t, x, \eta) d\eta.$$

The displacement appears in the self-warp component of our architecture while η labels the heads. As the equation is linear, Γ_{-t} does not depend on $u_{0,1}$.

Choosing (for a large H) the quadrature nodes $\eta_h \in \mathbb{S}^{d-1}$ and corresponding weights $w_h \in \mathbb{R}$, $h = 1, \dots, K$, we can approximate integrals over \mathbb{S}^{d-1} by a quadrature formula

$$\int_{\mathbb{S}^{d-1}} F(\eta) d\eta \approx \sum_{h=1}^H w_h F(\eta_h). \quad (24)$$

By using the quadrature (24) on \mathbb{S}^{d-1} to approximate the above integrals, we obtain

$$\begin{aligned} u(t, x) &\approx \int_{\mathbb{S}^{d-1}} W_0(t, x, \eta) u_0(x + \varrho(t, x, \eta)) J(t, x, \eta) d\eta + \int_{\mathbb{S}^{d-1}} W_1(t, x, \eta) u_1(x + \varrho(t, x, \eta)) J(t, x, \eta) d\eta \\ &\approx \sum_{h=1}^H W_0(t, x, \eta_h) u_0(x + \varrho_{t,h}(x)) J(t, x, \eta_h) w_h + \sum_{h=1}^H W_1(t, x, \eta_h) u_1(x + \varrho_{t,h}(x)) J(t, x, \eta_h) w_h, \end{aligned}$$

where $\varrho_{t,h}(x) = \Gamma_{-t}(x, \eta_h) - x$ are the displacement fields corresponding to the head η_h .

G. Related work on neural PDE learning

Early learning-based PDE solvers largely adopted CNN image-to-image backbones (Zhu & Zabaras, 2018; Bhatnagar et al., 2019; Pant et al., 2021), with U-Nets (Ronneberger et al., 2015) remaining a strong baseline due to their locality and multiscale structure. A parallel line of work frames PDE prediction as learning *solution operators* between (discretizations of) function spaces (Kovachki et al., 2023; Lu et al., 2021; Li et al., 2020). Within this operator-learning view, Fourier Neural Operators (FNOs) (Li et al., 2021; 2023) have been particularly influential: they use spectral mixing to realize global interactions and have become a standard reference point across benchmarks.

Following the success of Vision Transformers (Dosovitskiy et al., 2021), attention-based architectures have also been adapted to operator learning (Cao, 2021; Li et al., 2022). Their set-based formulations facilitate irregular meshes and complex geometries (Hao et al., 2023; Wu et al., 2024; Luo et al., 2025; Wen et al., 2025), but attention typically trades away strong locality priors and incurs quadratic scaling in the number of tokens, which is restrictive at high spatial resolution and in 3D. Hybrid models that mix multiple formalisms also exist (Guibas et al., 2022), aiming to combine global coupling with practical efficiency.

More recently, several works pursue foundation-model training for scientific dynamics: pretraining on diverse PDE families followed by task-specific finetuning (Subramanian et al., 2023; Herde et al., 2024; McCabe et al., 2024; Hao et al., 2024). These efforts are enabled by standardized benchmark suites and data collections, including PDEBench (Takamoto et al., 2024), PDEGym (Herde et al., 2024), and The Well (Ohana et al., 2025). In contrast to convolution-, Fourier-, or attention-based mixing, FLOWERS build global interactions from sparse, state-dependent *warps* (pullbacks) coupled with pointwise channel mixing, providing an explicit transport primitive that complements these prior approaches.